Aerodynamic Inverse Design of Turbomachinery Blading in Two-Dimensional Viscous Flow

Kasra Daneshkhah

Ph.D. Thesis

in

The Department

of

Mechanical and Industrial Engineering

Presented in Partial Fulfillment of the Requirements

for the Degree of Doctor of Philosophy at

Concordia University

Montréal, Québec, Canada

April 2006

Your file Votre référence
ISBN: 978-0-494-16295-8
Our file Notre référence
ISBN: 978-0-494-16295-8

ABSTRACT

Aerodynamic Inverse Design of Turbomachinery Blading in Two-Dimensional Viscous Flow

Kasra Daneshkhah, Ph.D.

Concordia Unviersity, 2006

An inverse blade design method, applicable to 2D and 3D flow in turbomachinery blading is developed and is implemented for the design of 2D cascades in compressible viscous flow. The prescribed design quantities are either the pressure distributions on the blade suction and pressure surfaces or the blade pressure loading and its thickness distribution. The design scheme is based on a wall movement approach where the blade walls are modified based on a virtual velocity distribution that would make the current and target momentum fluxes balance on the blade suction and pressure surfaces. The virtual velocity is used to drive the blade geometry towards a steady state shape corresponding to the prescribed quantities.

The design method is implemented in a consistent manner into the unsteady Reynolds Averaged Navier-Stokes (RANS) equations, where an arbitrary Lagrangian-Eulerian (ALE) formulation is used and the boundaries of the computational domain can move and deform in any prescribed time-varying fashion to accommodate the blade movement. A cell vertex finite volume method is used for discretizing the governing equations in space and, at each physical time level, integration in pseudo-time is performed using an explicit Runge-Kutta scheme, where local time stepping

and residual smoothing are used for convergence acceleration. For design calculations, which are inherently unsteady due to blade movement, the time accuracy of the solution is achieved by means of a dual time stepping scheme. An algebraic Baldwin-Lomax model is used for turbulence closure. The flow analysis method is applied to several test cases for steady state internal flow in linear cascades and the results are compared to numerical and experimental data available in the literature.

The inverse design method is first validated for three different configurations, namely a parabolic cascade, a subsonic compressor cascade and a transonic impulse turbine cascade, where different choices of the prescribed design variables are used. The usefulness, robustness, accuracy, and flexibility of this inverse method are then demonstrated on the design of an ONERA transonic compressor cascade, a NACA transonic compressor cascade, a highly cambered DFVLR subsonic turbine cascade, and a VKI transonic turbine cascade geometries, which are typical of gas turbine blades used in modern gas turbine engines.

ACKNOWLEDGEMENTS

I would like to express my deep and sincere gratitude to my supervisor, Professor Wahid S. Ghaly, at Concordia University, for his continued support, guidance and encouragement during this research.

I am very thankful to Professor Thong Dang for his time and effort in reviewing this work and providing valuable feedback.

I also wish to thank my friends and fellow students at Concordia University, especially Temesgen Mengistu and Wassim Basha for their friendship.

I am also grateful to my parents, for their love and encouragement throughout my entire life.

My final, and most heartfelt, acknowledgment must go to Tessa Awe. Her emotional support, encouragement, and companionship had turned my journey through graduate school into a pleasure.

TABLE OF CONTENTS

LIST OF FIGURES

LIST OF SYMBOLS

a	speed of sound
c	blade axial chord
D	discretized diffusive fluxes
c_p	specific heat in constant pressure
e	total energy per unit mass
f	blade camberline, general function
F,**G**	inviscid and viscous flux vectors
h	total enthalpy per unit mass
I	second order moment
k	thermal conductivity
L	pseudo-Laplace operator
n	surface normal vector
M	Mach number
p	static pressure
Q	discretized convective fluxes
Pr	Prandtl number
R	first order moment
R	residual vector
Re	Reynolds number
u	relative velocity vector
v	absolute velocity vector
u,v	cartesian velocity components
x,y	cartesian coordinates
s	displacement
t	time

T	temperature, blade thickness distribution
w	geometrical weights
w	vector of flow variables
α	flow angle, scaling coefficient
β	blade angle
δ	Kronecker delta function
Δ	difference
γ	ratio of specific heats
Γ	control volume boundary
κ^2, κ^4	constants associated with artificial viscosity terms
λ	eigen-value
ρ	density
μ	molecular viscosity
σ	stress tensor
ω	relaxation factor, vorticity
Ω	volume
ξ	mesh stretching direction
η	normal to mesh stretching direction

Subscripts

avg	average
e	edge
d	design (target)
g	grid
l	laminar
i,j	dummy indexes
max	maximum
n	normal

o	total or stagnation quantity of the flow
s	smoothing
t	turbulent
v	virtual

Superscripts

2,4	second and forth order
$\pm$	blade pressure and suction surfaces
n	new time step
o	old time step

Acronyms

ALE	Arbitrary Lagrangian-Eulerian
AV	Artificial Viscosity
CFD	Computational Fluid Dynamic
CFL	Courant-Fredrick-Lewy number
FVM	Finite Volume Method
LE,TE	Blade Leading and Trailing Edges
RANS	Reynolds Averaged Navier-Stokes

Chapter 1

Introduction

Aerodynamic analysis of the flow in blade row passages of modern gas turbine engines has been routinely performed by means of Computational Fluid Dynamics (CFD). However, aerodynamic design methods using main stream CFD techniques have not progressed as fast as analysis methods and have not been used as a common tool in the engineering practice. Some designers still adopt a direct (analysis) approach, evaluating the blade performance and modify the blade shape according to empirical rules or their own experience to obtain a target performance. This approach can be very time consuming, and even very inefficient in some cases.

More powerful design strategies for gas turbine blades can be obtained by means of optimization methods and inverse design methods. Numerical optimization methods [1, 2, 3] iteratively modify a set of geometrical parameters to achieve a certain objective function. The latter is computed from a CFD flow simulation. Numerical optimization methods can be combined with or implemented in any type of flow solver, but have the disadvantage of being very expensive in terms of computational time, because many flow analyses are usually required.

In situations where the detailed target performance is known, e.g., blade pressure loading or pressure distributions, inverse methods are probably the best approach to use. In the inverse shape design problem, the flow governing equations are recast such that the required detailed performance is prescribed and the corresponding blade shape and the flow field are obtained simultaneously as the part of the solution. The implementation of these methods requires modifications of the flow solver and/or boundary conditions. The computational time taken by the inverse methods is comparable with that taken by the analysis methods, which makes inverse methods less time-consuming than almost all optimization methods.

The main objective of this work is to develop an inverse design method for turbomachinery blading, which is applicable for 2D and 3D viscous flow. This requires development of a CFD code to simulate viscous flow equations using an accurate and efficient scheme and the development of an inverse method that can be directly implemented into the viscous fluid flow solver.

1.1 Turbomachinery Flow Analysis

The development of modern gas turbine engines with increased efficiency and reduced weight has led to the design of highly loaded compressor and turbine blades. The unsteady nature of the flow due to relative motion of the stator and rotor blades, 3D effects and turbulence are some of the major aspects which contribute to the flow analysis complexity. Figures 1.1 and 1.2 show the flow characteristics in a compressor and a turbine passage, respectively. As it can be seen, a detailed analysis of the flow requires a 3D viscous flow model, where the secondary flows, tip flows, end-wall boundary layers, etc., are simulated using appropriate boundary conditions.

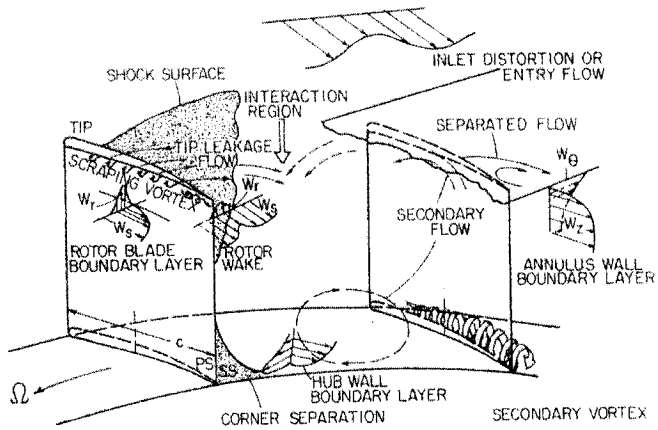

Figure 1.1: Flow characteristics in a compressor blade row
[taken form Lakshminarayana [4]]

Over the past few decades, with the rapid development of numerical methods and the availability of powerful computers, efficient codes are developed for simulation of the flow in multi-stage compressors and turbines [5, 6, 7, 8]. These investigations use a time-accurate solution of the unsteady governing equation, where the computational grid is divided into stationary parts for stator blades and moving parts for rotor blades. Special treatment of the interface of the stationary and moving grids is required for the analysis of the subsequent blade rows interactions, while ensuring the conservation of the computational procedure. The fluid flow governing equations can be extended to account for moving grids using an Arbitrary Lagrangian-Eulerian formulation, originally developed for external flow aeroelasticity analysis [9, 10]. For turbomachinery applications, this formulation is very useful for any type of unsteady calculation on moving girds, such as rotor/stator interaction [7, 11], turbomachinery aeroelasticity [12], dynamic response predictions of stall flutter [13, 14, 13] and mistuning effects [11, 15].

Most of the aerodynamic studies on gas turbine blades, including experimental

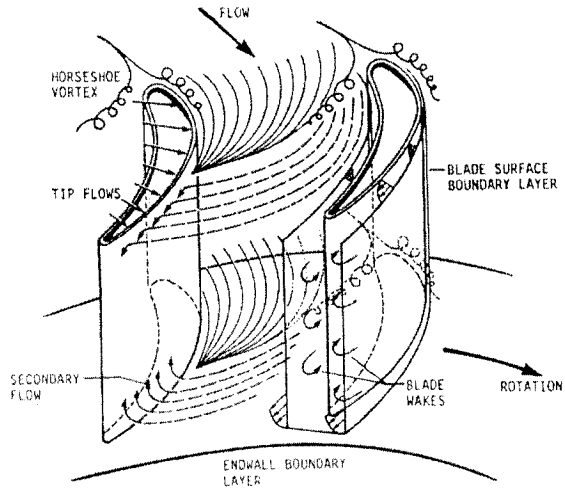

Figure 1.2: Flow characteristics in a turbine blade row
[courtesy of NASA-Lewis Research Center]

as well as numerical approaches, are traditionally performed on blade cascades. A compilation of experimental data for CFD validation can be found in Fottner [16]. Numerical simulations, in this regard, include the solution of Euler or Navier-Stokes equations in 2D cascades [17, 18, 19, 20] and 3D cascades [21, 22, 23, 5]. While 3D cascade flow solvers are needed to obtain more realistic results and detailed flow field solution, a 2D cascade solver is a desirable tool for many applications. They provide fast and accurate results compared to their 3D counterparts. Hence, they can be used for development and assessment of numerical schemes [17, 19, 24, 25]. The 2D cascade flow exhibit several flow phenomena typical of turbomachines, such as coexistence of subsonic, transonic and supersonic flow, shock waves and their interaction with boundary layers and wakes, and flow separation. Although the viscous effects are confined to thin regions near the walls and wakes, the presence of boundary layers can have a drastic influence on the flow pattern. In the transonic

regime, the viscous effects can cause the location of the shock to shift by as much as 20% chord [26]. Depending on the strength of the shock wave, the interaction between the shock and boundary layer can cause massive separation of the flow at the shock foot with a subsequent rise in drag and pressure losses. Furthermore, the characteristics of the blade at stall are entirely determined by viscous phenomena. To properly simulate viscous flow details, special care should be given to both the solver and the computational grid that are used.

1.1.1 Present Analysis Method

For the flow analysis in the present study, the compressible viscous flow in 2D cascades are simulated by solving Reynolds-Averaged Navier-Stokes equation using a cell-vertex finite volume method on fully unstructured triangular meshes. The code that was originally developed by Ahmadi [27] for invicid flow in 2D cascades is modified to include the viscous effects. The method uses an explicit Runge-Kutta time-marching procedure to obtain the steady state solution, where local time-stepping and implicit residual smoothing are employed for convergence acceleration. The non-linear artificial viscosity formulation advanced by Jameson *et al.* [28], combined with the pseudo-Laplacian discretization introduced by Holmes and Connel [25] are used for numerical stability and to capture discontinuities. The inflow and outflow boundary conditions are based on a linearized one-dimensional characteristic method [29]. Improvements in the flow analysis code include proper treatment of the viscous and artificial dissipation terms on highly stretched meshes, which are required for viscous flow simulation, and implementation of the Baldwin-Lomax turbulence model [30] for the closure of the governing equations. In anticipation for the proposed inverse method, developed in this thesis, the ALE formulation for

moving grids and the time accurate solution scheme using dual time stepping [31] are also implemented. The numerical method used for discretization and solution of the flow governing equations is presented in details in Appendix A. Validation of the code for steady-state laminar and turbulent flow in turbomachinery cascades is presented in Appendix C. The results show that the method is reliable and accurate for the solution of viscous flow equations in 2D cascade flows.

1.1.2 Grid Generation Considerations

Although the external flow application is dominated by the unstructured grids [32, 33], most turbomachinery methods use a structured mesh [34, 35]. While unstructured grids provide flexibility for discretizing complex geometries, they have the drawback of requiring more memory and more CPU time than their structured counterparts. However, the requirement to include complex geometry features such as thick LE/TE, high stagger angle blading, tip gaps, cooling holes, etc., suggests the use of unstructured meshes as a suitable alternative for turbomachinery applications. They can also be easily and naturally coupled to mesh adaptation routines, to increase the efficiency and accuracy of the solution scheme [20].

An unstructured grid is used in this work for discretization of the computational domain. These grids are relatively easy to generate and efficient for capturing the inviscid features of the flow. However, the situation is more complicated for viscous flow computations, where large aspect ratio cells are required for to capture the details of the flow field in the boundary layers. The gradients of flow variables normal to the wall are several order of magnitudes larger than those along the wall; thus more grid points are required in the former direction than the latter. Hence isotropic unstructured meshes with no preferred direction are not appropriate for

viscous flow computations.

In this work a hybrid grid is used for viscous flow computations, where the boundary layers are filled with a structured mesh and the rest of the domain is filled with triangular elements. Each quadrilateral element is divided into two triangles and the mesh is represented to the solver as an edge-based data structure. Consequently the solver has a unified data structure for which the nature of the hybrid mesh is concealed from the main calculation loops. A similar approach can be extended to 3D flows. Figure 1.3 shows the computational domain and the hybrid grid for a typical 2D subsonic turbine cascade.

1.2 Inverse Design Approach

In the analysis approach, the performance of a given blade geometry is obtained from the solution of the flow governing equations. An alternative to this approach is inverse shape design problem, where the blade performance is prescribed and the corresponding geometry is obtained as part of the solution. The primary goal of inverse design is to determine the blade shape that would achieve a target blade pressure distribution or a target pressure loading, while the computational time is comparable to analysis. Inverse techniques for turbomachine blades are used in industry, but they are far from being at the sophistication level of the analysis methods.

1.2.1 Previous Investigations

First generation of the inverse methods are analytical solutions of potential flow equations, developed by Lighthill [36] and Sanz [37]. These methods are limited to shock free irrotational flows and are difficult to extend to three dimensions. In the

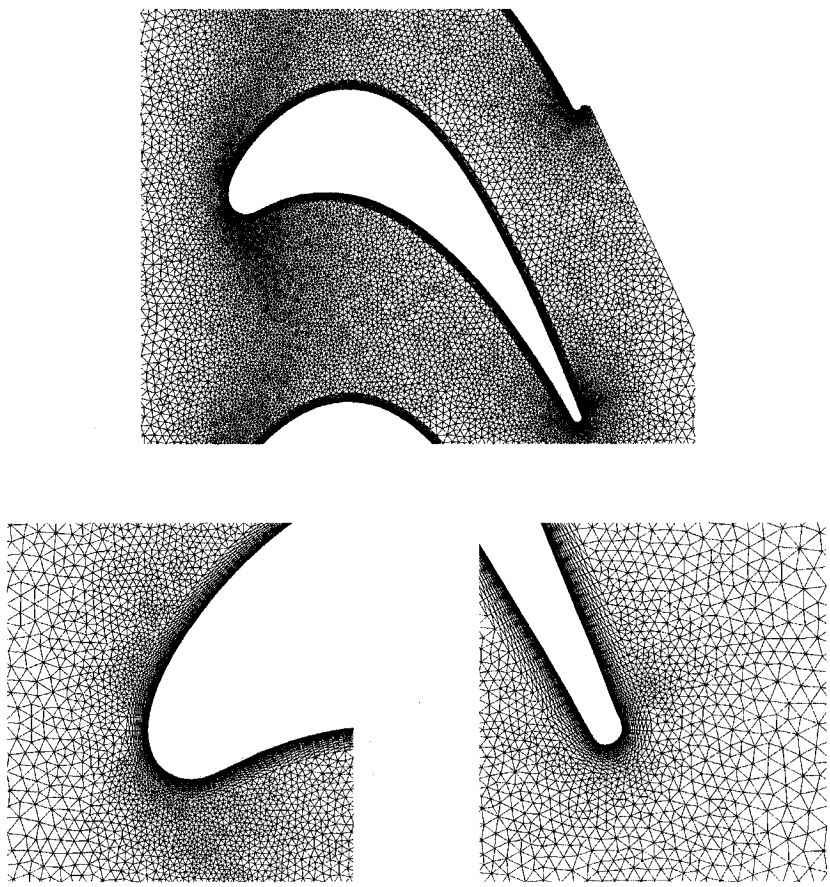

Figure 1.3: The hybrid mesh for a transonic turbine blade.

last two decades, inverse methods have been developed and implemented into CFD codes that solves the Euler or Navier-Stokes equations. Some of these methods are summarized in this section.

The inverse design method of Leonard and Van den Braembussche [38] and Demeulenaere and Van den Braembussche [39, 40] solve the time-dependent Euler equations in a computational domain, where some boundaries (the blade walls) move during the transient part of the computation. The geometry modification algorithm is based on a transpiration principle, where a normal velocity distribution is computed from the difference of actual and prescribed pressure distributions, to approximate the position of the two streamlines starting from the stagnation point. These streamlines form the new blade profile. The method is successfully applied to inviscid flow problems but when applied to viscous flow case, a representative velocity at the edge of the boundary layer is required [41], which can be difficult to identify in internal flow. Recently that method has been reworked for viscous flow where a Navier-Stokes solver for the flow analysis is blended with a Euler solver for the inverse design [42].

The inverse design method proposed by Hawthorne *et al.* [43] designs blade with a prescribed mean average swirl distribution throughout the meridional section of the machine. Dang [35] extended this method to transonic flows in radial and mixed flow machines, such that the blade mass-averaged swirl schedule (which is proportional to pressure jump across the blade) and thickness distribution are prescribed. He implemented the method into Euler equations which he solved using a cell-centered finite volume scheme and applied the method to 2D cascades [44] and 3D cascades [45] in transonic flow regime. Medd [46] and Medd and Dang [47] also adapted this method for 2D and 3D blade design using viscous flow equations, where

a Baldwin-Lomax model was used for turbulence closure. Ahmadi and Ghaly implemented a similar method for inviscid flow using a cell-vertex finite-volume method on unstructured meshes [20] and applied the method to design transonic shock-free compressor cascades [27]. Zangeneh [48] also used this method for 3D design of centrifugal compressor cascade, where he introduced the viscous effects indirectly by an inviscid/viscous interaction.

In the above mentioned inverse methods, the blade tangency condition, which is true only for inviscid flow, is an integral part of the formulation. Therefore, these methods are not directly applicable to viscous flows.

The inverse method proposed by Thompkins and Tong [49] uses the pressure distributions on the blade surfaces, where a steady state time-marching solution scheme with shock capturing technique is used for the solution of the Euler equations. This method is based on a wall movement with a virtual velocity calculated from the balance of momentum fluxes on the blades surfaces, which can be readily applied to viscous flow equations as it does not invoke any tangency condition on the blade surface. They applied the method to design 2D transonic compressor cascades [50]. The only application of this method to viscous flow problems is reported by Yang and Ntone [51]. They manually coupled the geometry modification technique with a steady-state Navier-Stokes solver for the flow analysis and applied the method to a nozzle design problem and a subsonic compressor cascade design. The results show a closer approximation of the target pressure distribution after a limited number of geometry modifications.

1.2.2 Present Inverse Design Method

In the present inverse design method, the wall movement concept originally proposed by Thompkins and Tong [49, 50], is adopted and the unsteady flow associated with the blade motion is simulated numerically by solving the Navier-Stokes equations using a cell-vertex finite volume space discretization coupled with an ALE formulation to account for the moving and deforming computational domain. Marching in time is accomplished using a time-accurate implicit time stepping scheme. The design variables are specified as either the pressure distribution on the blades suction and pressure sides, or the blades pressure loading and their thickness distribution. The design method is validated and assessed for inviscid and viscous flow cascades, and is then applied to the design of compressor and turbine cascades in 2D subsonic and transonic flow regimes; these cascades are typical of those currently used in the gas turbine industry.

1.3 Thesis Outline

This work is organized into five chapters, including this introduction. In the second chapter, the RANS equations and the boundary condition for 2D cascade flow are presented along with the description of the ALE formulation for moving grids followed by Space Conservation Law which is used to compute the grid velocity field.

Details of the numerical method used for discretization and solution of the flow governing equations are given in Appendix A. Validation of the code for steady-state laminar and turbulent flow in turbomachinery cascades is presented in Appendix C.

Chapter three presents the inverse design formulation and implementation in details and discusses the issues such as stability of the scheme and different choices of design variables. The design method is validated and accessed for inviscid and

viscous flow cases in the subsonic and transonic flow regimes, using different choices of design variables.

In chapter four, the design method is applied to 2D compressor and turbine blade cascades, which are typical of those currently used in the gas turbine industry. The usefulness and practicality of the method are emphasized on a number of difficult design cases available in the literature.

Finally chapter five presents the conclusion, where the main achievements and findings of this work are summarized, followed by recommendations for future work.

Chapter 2

Flow Simulation Method

In this chapter, the governing equations of compressible viscous flow are presented using an arbitrary Lagrangian-Eulerian (ALE) formulation, where the domain boundaries can move and deform in any time-varying fashion. This formulation is used for inverse design calculations, where the blade motion is enforced by the design scheme. The steady state solution of the governing equations for a stationary computational domain are simply recovered by neglecting the grid velocities.

Through out this work, the appellation "Navier-Stokes" or "Euler" equations loosely refers to the flow governing equations, i.e, the system consisting of continuity, momentum, and energy equations. In the limit of negligible viscosity, the Euler equations are recovered and, in some cases, they are solved instead of the Navier-Stokes equations, given their lower computational cost.

Details of the numerical method used for discretization and solution of the flow governing equations are given in Appendix A. Description of the turbulence model used for the closure of the Reynolds Averaged equations is given in Appendix B. Validation of the code for steady-state laminar and turbulent flow in turbomachinery cascades is presented in Appendix C.

2.1 The Governing Equations

The motion of a compressible turbulent flow can be described by Reynolds Averaged Navier-Stokes (RANS) equations. These equations can be cast in terms of absolute velocity $\mathbf{v}$ but solved in a non-inertial relative reference frame, using an ALE formulation for a domain with time-dependent boundaries. The integral form of the RANS equations for an arbitrary control volume $\Omega(t)$, bounded by the surface $\Gamma(t)$, written in vector notation is as follows:

$$\frac{\partial}{\partial t}\iint_{\Omega} \mathbf{w}\, d\Omega + \oint_{\partial\Omega} \mathbf{F}\cdot\mathbf{n}\, d\Gamma = \frac{1}{Re}\oint_{\partial\Omega} \mathbf{G}\cdot\mathbf{n}\, d\Gamma \tag{2.1}$$

where $\mathbf{n}$ represent outward unit vector of the control volume boundary $\Gamma(t)$.

The solution vector of conservative variables $\mathbf{w}$ is given by

$$\mathbf{w} = \begin{bmatrix} \rho \\ \rho\mathbf{v} \\ \rho e \end{bmatrix} \tag{2.2}$$

and the inviscid flux vector $\mathbf{F}$ has the following components

$$\mathbf{F} = \mathbf{w}\mathbf{u} + \begin{bmatrix} 0 \\ p\delta_{ij} \\ v_j p \end{bmatrix}. \tag{2.3}$$

Here δ_{ij} represent the Kronecker delta function and $\mathbf{u} = \mathbf{v} - \mathbf{v}_g$ is the velocity in the relative frame of reference. For an ideal gas, thermally and calorically, the pressure p and the total enthalpy h are related to density ρ, absolute velocity $\mathbf{v}$ and internal energy e

$$p = (\gamma - 1)\rho\left[e - \frac{|\mathbf{v}|^2}{2}\right], \quad h = e + \frac{p}{\rho} \tag{2.4}$$

where γ is the constant specific heat ratio. The viscous flux vector $\mathbf{G}$ on the right hand side of the Eq. 2.1 is scaled by the reference Reynolds number for Non-dimensional purposes and has the following components:

$$\mathbf{G} = \begin{bmatrix} 0 \\ \sigma_{ij} \\ v_k \sigma_{ik} + \frac{\gamma}{\gamma - 1} \left(\frac{\mu_l}{Pr_l} + \frac{\mu_t}{Pr_t} \right) \frac{\partial T}{\partial x_i} \end{bmatrix}. \tag{2.5}$$

The viscous stress tensor σ_{ij} is expressed using the eddy viscosity concept which assumes that, in analogy with viscous stress in laminar flows, the turbulent stresses are proportional to mean velocity gradients:

$$\sigma_{ij} = \mu \left(\frac{\partial v_i}{\partial x_j} + \frac{\partial v_j}{\partial x_i} \right) + \lambda \delta_{ij} (\nabla \cdot \mathbf{v}) \tag{2.6}$$

where μ_l represents the molecular viscosity, μ_t denotes the turbulent eddy-viscosity, which must be determined by a suitable turbulence model. Therefore, $\mu = \mu_l + \mu_t$ is the total viscosity of the fluid. The value of λ is given by the Stokes relation $\lambda = -\frac{2}{3}\mu$, while the laminar Prandtl number Pr_l is taken is 0.7 for air. The turbulent Prandtl number, Pr_t, is taken as 0.9.

In this work, an algebraic Baldwin and Lomax model [30] is implemented for the closure of the governing equations for its simplicity and success in simulating turbomachinery flows [52, 53]. Description of the turbulence model and details of implementation are given in Appendix B.

2.2 Arbitrary Lagrangian-Eulerian Formulation

The Arbitrary Lagrangian-Eulerian (ALE) form of the governing equations are derived by replacing the partial derivative with respect to time of any quantity f with

the ALE time derivative, given by:

$$\frac{\partial f}{\partial t} = \frac{df}{dt} - \mathbf{v}_g \cdot \nabla f, \tag{2.7}$$

where $\mathbf{v}_g = \frac{d\mathbf{x}}{dt}$ is the the grid velocity field. By taking $\mathbf{v}_g = \mathbf{v}$, the Lagrangian description of flow is obtained. On the other hand,$\mathbf{v}_g = 0$ on a stationary grid and the Eulerian description of flow is recovered. In the Eulerian framework, on moving meshes, the domain must be remeshed and the solution must be interpolated at every time step to account for the deformation of the computational fluid domain which conforms to the moving structure.

In the ALE formulation, the nodes on the body move at the speed of the moving and deforming body, with the interior grid points moving in arbitrary fashion, but is such a way as to prevent mesh tangling. Further, the flow variables are advanced in time along the nodal trajectories without the need for an explicit interpolation step. In finite volume implementation, the new term $\mathbf{v}_g \cdot \nabla f$ is lumped with the convective term $\nabla \cdot (f\mathbf{v})$ to take the form $\nabla \cdot [f(\mathbf{v} - \mathbf{v}_g)]$ ($f = \rho$ for continuity, $f = \rho\mathbf{v}$ for momentum, $f = \rho e$ for energy). Although a source term arises from this formulation, this formulation is required for the conservation calculation of the unsteady fluxes on the moving grids, with the fluid moving through the cell at a relative convective velocity $\mathbf{u} = \mathbf{v} - \mathbf{v}_g$.

2.3 Space Conservation Law

The movement of the coordinate system results in an additional conservation equation, which has to be satisfied simultaneously with the other conservation equations. This equation follows from the fact that the coordinate frame velocities have to conserve space at the local and global levels at all times and hence is called "Space

Conservation Law" (SCL). For a uniform flow with zero velocity, the integral form of the continuity equations results in the SCL equation:

$$\frac{d}{dt}\iint_{\Omega} d\Omega + \oint_{\Gamma} \mathbf{v}_g.\mathbf{n}d\Gamma = 0 \tag{2.8}$$

where $\mathbf{v}_g = (u_g, v_g)$ is the cell face velocity and $\mathbf{n} = (n_x, n_y)$ is the cell face normal vector. The grid velocities must therefore be defined in such a way that the integral of $\mathbf{v}_g.\mathbf{n}$ equals the volume change of the control volume. If this relation is not respected, artificial mass sources or sinks are introduced, leading to instabilities [54, 55]. Further details on discretization of this equation and computation of the grid velocities are presented in Appendix A.

2.4 Additional Driving Terms

As mentioned in Sec. 2.2, the ALE form of governing equations for a finite volume method results in additional source terms which must be accounted for while integrating the equations in time. If the time derivative is split into two terms, the discretized form of the mass conservation equations becomes:

$$\Delta\rho = \sum_{k} \left[\rho\mathbf{v}\cdot\mathbf{n} - \left(\rho\mathbf{v}_g\cdot\mathbf{n} + \rho\frac{\Delta\Omega}{\Delta t}\right)\right]\frac{\Delta t}{\Omega} \tag{2.9}$$

The first right-hand side term is the residual for a fixed mesh, while the two additional terms are due to the mesh movement. Their physical meaning is easily explained. The convective fluxes must be measured using relative velocity, obtained by subtracting the mesh velocity from fluid velocity, resulting in the first additional term. The convective fluxes entering the control volume cause a variation of mass in the control volume, which is the product of *density* $\times$ *volume*. In the case of moving grids, both can change, which explains the presence of the second additional term.

In the frame of inverse method, the two additional terms resulting from the mesh movement converge to zero at steady state. Moreover, it is clear that the two terms should compensate each other in smooth flows. It could be concluded from this that the presence of those terms is not necessary for steady computations, as proposed by Demirdzic and Peric [54]. However, experience has shown that these additional terms are essential for obtaining a satisfying convergence rate of the computations at transonic flow conditions with shocks [41].

2.5 Boundary Conditions

For a cascade problem, there are four types boundary condition, namely inflow/outflow boundary conditions, periodic boundary conditions and solid wall boundary conditions, which must be enforced along the boundaries of the computational domain. Figure 2.1 shows the computational domain and the boundary conditions for a typical 2D turbine cascade.

The computation of inflow and outflow boundary conditions is based upon a linearized characteristics method, described in [29]. The change in the incoming characteristics are determined such as to satisfy specified boundary conditions. For a subsonic inflow, there are three characteristics propagating into the domain and only one outgoing. The flow angles, stagnation enthalpy and stagnation pressure are specified at the inflow and the static pressure is extrapolated from inside the domain. In some cases the reduced mass flow rate is specified at the inlet boundary. There are four incoming waves for a supersonic inflow. The Mach number is also specified for a supersonic inflow and subsequently the flow condition will be determined from these variables using isentropic relations. For subsonic outflow, three outgoing waves are calculated from the numerical solution, while the incoming wave is fixed by specifying

the static back pressure. There are four outgoing waves for a supersonic outflow, hence all the flow variables are extrapolated from inside the domain.

The flow periodicity for a linear cascade implies that all the variables are the same at periodic pairs of nodes. To avoid interpolation and accompanying inaccuracy, the grid generation provides the periodic nodes in pair, which are treated as interior nodes by adding all the contributions at one periodic node to its periodic counterpart.

Finally, the solid wall boundary conditions are modified to account for the moving boundaries. For the Navier-Stokes equations, the no slip boundary condition $\mathbf{v} = 0$ at a wall becomes $\mathbf{v} = \mathbf{v}_g$. For the Euler equations, the flow tangency condition $\mathbf{v} \cdot \mathbf{n} = 0$ becomes $\mathbf{v} \cdot \mathbf{n} = \mathbf{v}_g \cdot \mathbf{n}$. Any deformation or motion of the structure is thus reflected in the flow boundary conditions and will be accounted for in the flow solution.

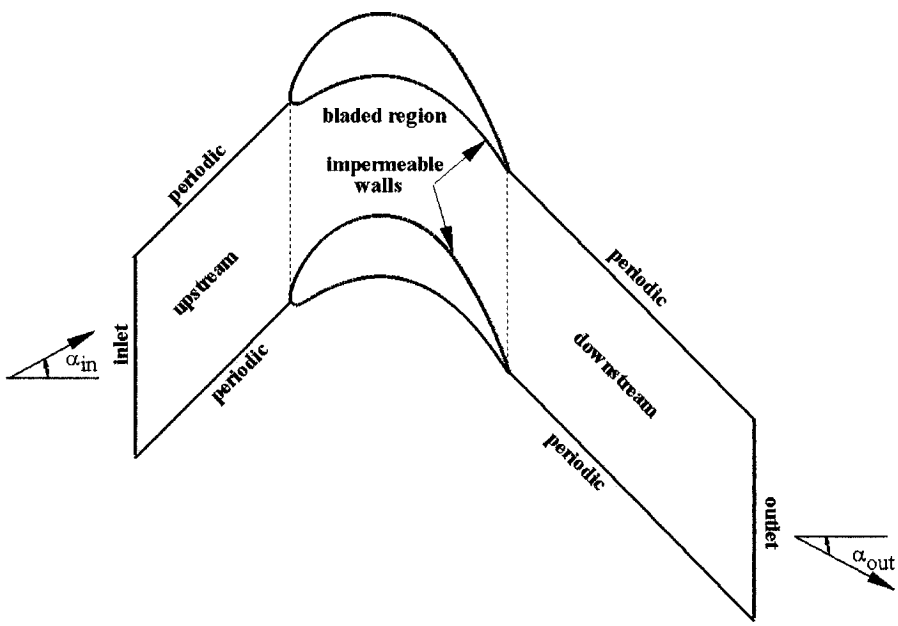

Figure 2.1: Computational domain and boundary conditions

Chapter 3

Inverse Design Method

In this chapter, the inverse design methodology is presented and is validated for 2D inviscid and viscous flow in turbomachinery cascades. The inverse design scheme is basically a time accurate solution of the RANS or Euler equations, where the blade geometry is modified iteratively to accomplish the prescribed performance. The governing equations, which are expressed in ALE form, allow for the movement and deformation of the computational grid during the design process. The blade motion is enforced by a virtual blade velocity that is derived from a balance of momentum fluxes on the blade surfaces. The target performance is prescribed by specifying either the pressure distribution on both surfaces, i.e. the blade pressure and suction surfaces, or the pressure loading and blade thickness distribution. Several validation cases are presented to demonstrate the flexibility and robustness of the scheme as well as consistency of the design and analysis solutions.

3.1 Choice of Design Variables

The present inverse design method allows for specification of either pressure distributions on the blade pressure and suction surfaces or pressure loading and thickness distribution of the blade as prescribed design variables. The specification of the blade loading distribution as the aerodynamic design input is more convenient from a designer's point, particularly in 3D flows where the designer has a better knowledge of a good choice of pressure loading compared to pressure distribution on the blade surfaces. Moreover the prescription of the blade thickness distribution guarantees that the blade shape is closed and provides more control over the blades structural and manufacturing feasibility.

The design scheme requires a target pressure distribution $p_d^{\pm}$ on the blade surfaces to derive the geometry modifications. In cases where a target pressure loading Δp_d is specified, the pressure distributions on the blade surfaces can be computed at each time step as:

$$p_d^{\pm} = p_{avg} \pm \Delta p_d \tag{3.1}$$

where

$$p_{avg} = \frac{1}{2}(p^+ + p^-). \tag{3.2}$$

and $p^{\pm}$ refer to the pressure on the $\pm$ sides of the blade, as shown in Fig. 3.1, that are computed from the time-accurate solution of the governing equations.

In some cases, Eq. 3.1 may result in a non-physical value ($p_d^+ > 1$) during the design process. For such cases, given that the pressure distribution on the pressure side is usually less sensitive to changes in geometry, the target pressure distributions

can be taken as:

$$\begin{aligned} p_d^+ &= p^+ \\ p_d^- &= p^+ - \Delta p_d \end{aligned} \tag{3.3}$$

where the target pressure distribution on the pressure side p_d^+ is taken to be the same as the one obtained from the time-accurate solution during the design process and is used with the target loading Δp_d to compute the target pressure distribution on the suction side p_d^-.

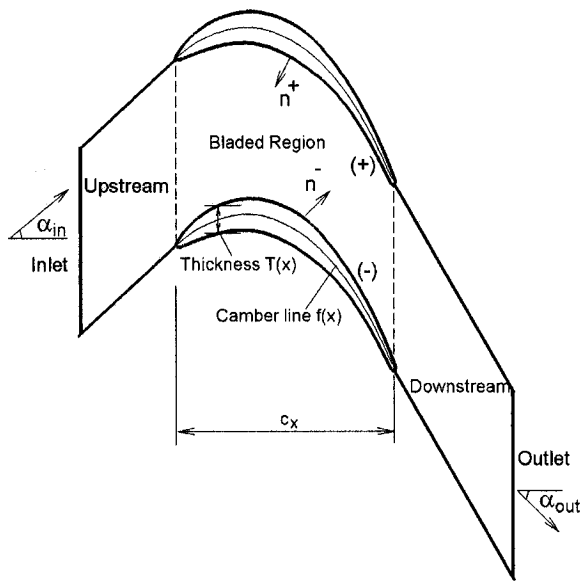

Figure 3.1: Cascade notation and computational domain.

3.2 Inverse Design Formulation

The wall movement approach is used to change the blade profile so as to satisfy the prescribed blade pressure distributions. The blade motion is enforced by a virtual velocity distribution, which is derived from the difference between the actual and target pressure distributions on the blade surfaces. The virtual velocity distribution, $\mathbf{v}_v^{\pm} = (u_v^{\pm}, v_v^{\pm})$ on the $\pm$ sides of the blade, are derived such that the corresponding virtual momentum flux on the blade $\pm$ surfaces would be equal to a design momentum flux, that is:

$$\begin{aligned} \left(\rho u_v^{\pm} u_v^{\pm} + p^{\pm}\right) n_x^{\pm} + \left(\rho u_v^{\pm} v_v^{\pm}\right) n_y^{\pm} &= p_d^{\pm} n_x^{\pm} \\ \left(\rho u_v^{\pm} v_v^{\pm}\right) n_x^{\pm} + \left(\rho v_v^{\pm} v_v^{\pm} + p^{\pm}\right) n_y^{\pm} &= p_d^{\pm} n_y^{\pm} \end{aligned} \tag{3.4}$$

where $\mathbf{n}^{\pm} = (n_x^{\pm}, n_y^{\pm})$ are the vectors normal to the $\pm$ surfaces. Equation 3.4 implies that there is a blade profile that would match the prescribed pressure distributions, hence as the solution advances in time, the initial blade profile will be changed gradually towards the sought blade profile and the virtual velocity will eventually vanish.

The above equations can be solved directly to obtain the virtual velocity components, which leads to:

$$\begin{aligned} v_v^{\pm} &= \pm \left(\frac{n_y^{\pm 2}}{n_x^{\pm 2} + n_y^{\pm 2}} \frac{|p_d^{\pm} - p^{\pm}|}{\rho^{\pm}} \right)^{\frac{1}{2}} \\ u_v^{\pm} &= v_v^{\pm} \frac{n_x^{\pm}}{n_y^{\pm}} \end{aligned} \tag{3.5}$$

where the signs of $u_v^{\pm}$ and $v_v^{\pm}$ are chosen such that an excess predicted pressure is balanced by a positive wall velocity. A virtual velocity distribution in the direction normal to the wall can then be calculated from:

$$v_{n,v}^{\pm} = \mathbf{v}_v^{\pm} \cdot \mathbf{n}^{\pm} \tag{3.6}$$

the wall displacement correction $\delta s^{\pm}$ is proportional to $v^{\pm}_{n,v}$ but in the opposite direction since the no-penetration condition implies that relative velocity normal to the wall is always zero, so that

$$\delta s^{\pm}_{e} = -\omega \, \Delta t \, v^{\pm}_{n,v} \tag{3.7}$$

where $\delta s^{\pm}_{e} = (\delta x^{\pm}_{e}, \delta y^{\pm}_{e})$ is the displacement of each edge on the blade walls in normal direction, Δt is the user defined physical time step, and ω is a relaxation factor that is determined based on stability requirements. The stability analysis [49], given in Appendix D, shows that the wall update scheme should be strongly under-relaxed. Typical values for the under-relaxation factor ω are 0.2 for subsonic flows and 0.04 for transonic flows.

The modified blade geometry is constructed by applying the wall displacement on discrete grid points on the blade surfaces, that is:

$$\begin{aligned} x^{n\pm}_{e} &= x^{o\pm}_{e} + \delta x^{\pm}_{e} \\ y^{n\pm}_{e} &= y^{o\pm}_{e} + \delta y^{\pm}_{e} \end{aligned} \tag{3.8}$$

where superscripts n and o denote the new and old blade geometry. Figure 3.2 shows the schematic of the wall movement. The resulting blade profile is scaled to preserve the axial chord length, and the grid points on the blade surface are interpolated back to the same axial location, hence the computational grid is essentially moving in y-direction.

A smoothing of the resulting blade profile is also essential to provide a smooth blade profile [49] and is given by:

$$y^{\pm}_{j} = y^{\pm}_{j} + \omega_{s}[|y^{\pm}_{j+1} - y^{\pm}_{j}|(y^{\pm}_{j+1} - y^{\pm}_{j}) + |y^{\pm}_{j-1} - y^{\pm}_{j}|(y^{\pm}_{j-1} - y^{\pm}_{j})] \tag{3.9}$$

where j refers to discrete grid points on the blade surface. The correct wall geometry for arbitrary input pressure may not be as smooth as required by Eq.3.9,

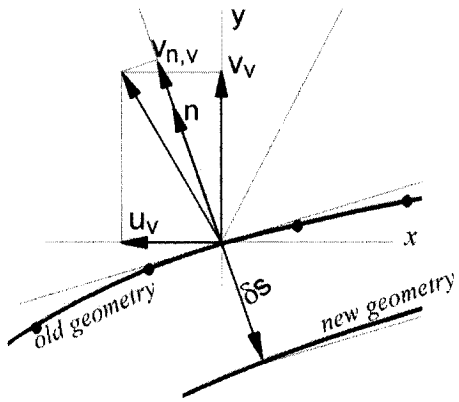

Figure 3.2: schematic of the wall movement

and a real position error may be introduced. A careful balance must be maintained between smoothing out the profile and producing a geometry that does not satisfy the specified pressure distribution but is as smooth as requested. The value of ω_s is determined by numerical experimentation, a typical value that was used in all cases presented in this work is $\omega_s = 0.2$.

For the cases where the blade loading and thickness distributions are prescribed, the average displacement of $\pm$ surfaces is applied to the blade camberline and the blade profile is constructed by combining the prescribed tangential thickness distribution and the modified camberline as follows:

$$y^{\pm} = f(x)^n \pm \frac{1}{2}T(x)^o \tag{3.10}$$

where

$$f(x)^n = f(x)^o + \frac{1}{2}(\delta y^+ + \delta y^-) \tag{3.11}$$

The blade smoothness is achieved by smoothing the blade camberline, similar to Eq.

3.9. To avoid unnecessary interpolations, the grid points on the blade surfaces are positioned as pairs of nodes with the same axial locations on the $\pm$ surfaces.

We note that the derivation is valid for inviscid and viscous flow. Although the contributions of viscous terms to the flux balance Eq. 3.4 are neglected, the results have suggested that a balance of convective terms is sufficient to drive the wall towards a shape that satisfies the target blade pressure distribution.

3.3 Grid Displacement and Velocity

The grid displacement adjusts the computational grid such that it follows the deformation of the blade profile, given in Eqs. 3.9 and 3.10, and is depicted in Fig. 3.3. A number of grid movement strategies are reported in the literature. The mesh can be moved either using an algebraic mapping, a smoothing operator, or global remeshing. In the present work, the grid movement is implemented through an algebraic mapping namely transfinite interpolation. This method has the ability to regenerate the new grid at relatively low computational cost.

From the calculated grid displacement, the grid velocity field $\mathbf{v}_g$ is computed from the Space Conservation Law (SCL) (see Eq. A.14. This grid velocity field is then substituted into the flow governing equations, Eq. A.4.

3.4 Inverse Design Algorithm

The wall movement algorithm described in the previous section is implemented into RANS equations using an ALE formulation, where a time accurate solution is obtained on a time-varying blade geometry during the design calculation. Each geometry modification step is considered to occur in a physical time step Δt.

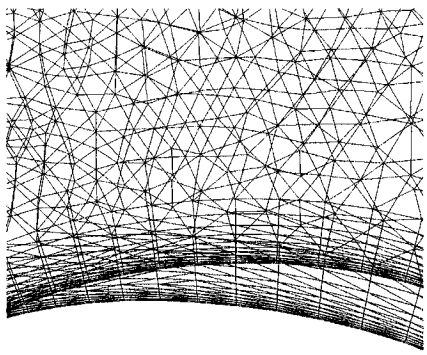

Figure 3.3: Grid movement

The design procedure starts from a steady state converged solution on a trial geometry and either a target pressure distribution on the blade surfaces or the blade pressure loading and its thickness distribution. Since a trial geometry does not satisfy the prescribed pressure distribution, a virtual velocity distribution is computed from the difference between the actual and target pressure distributions. The blade profile is then modified using the normal component of the virtual velocity.

After the blade geometry is modified, the computational grid is adjusted to accommodate the displacements of the domain boundaries. The grid velocity field is computed from the SCL, which ensures the conservation of the space during the solution.

The time accuracy of the solution is obtained by means of a dual time-stepping scheme, described in details in Appendix A. The pressure distribution is obtained on the modified blade geometry and the procedure is repeated until the target pressure distribution is reached. The convergence of the inverse design problem is monitored by the L_2 norm of the mesh displacement. When this value decreases with time until

it reaches the desired tolerance, then a steady state condition is practically reached and the target pressure distribution is achieved on the latest blade geometry. The results have suggested that convergence of the L_2 norm of the mesh displacement by two to three orders of magnitude ensures that the pressure field is not affected by the grid velocities, i.e. a steady state solution can be practically assumed. The overall computational time for an inverse calculation depends on the number of geometry modifications and the time required to obtain the time accurate solution after each geometry modification. For most cases, the L_2 norm of the continuity equation is decreased to 10^{-6} after each geometry modification. This level of convergence is found to be sufficient for the time accuracy and stability of the design scheme. Figure 3.4 shows the flow chart of the design algorithm.

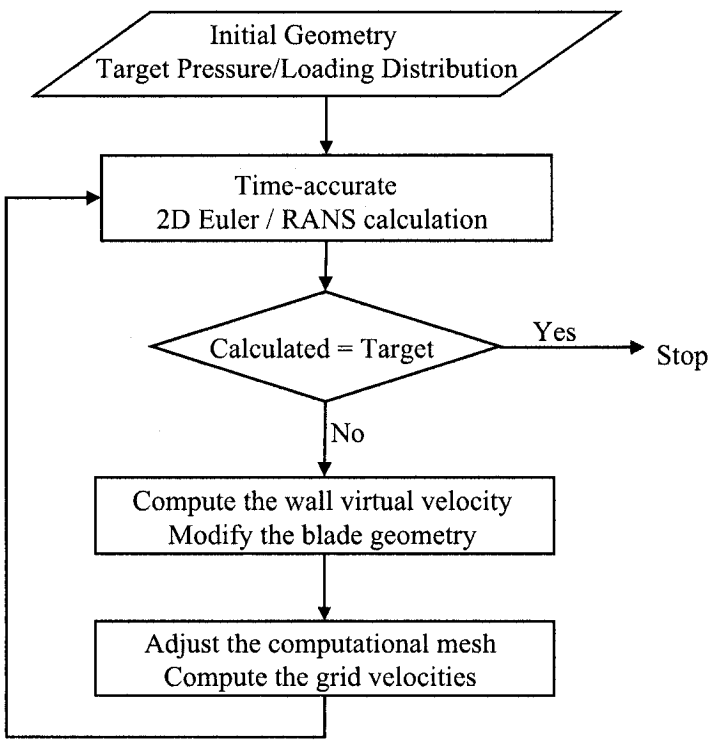

Figure 3.4: Computation algorithm for inverse design

3.5 Constraints

In a compressor or turbine design cycle, the detailed blade shapes are obtained towards the end of the design however these shapes must satisfy several geometric and non-geometric constraints. Some of these constraints can readily be satisfied in the proposed inverse method, e.g. the blade chord, number of blades, blade shape near the leading and trailing edges, the specific work or overall turning, inlet flow angle, reduced mass flow rate (or inlet total pressure), inlet total temperature, and exit static pressure.

All geometric constraints can be imposed directly through geometry construction. Prescribed LE/TE shapes extending between 1 and 3% chord at both blade ends, can be obtained by imposing a specific geometry in the blade LE and/or TE regions. This is accomplished by matching the blade thickness and camberline with that obtained from the design calculation at the junction points, thus ensuring that the blade LE/TE shapes are closely controlled. However, the specified blade pressure distributions will not necessarily be achieved in these regions (that extend between 1 and 3% chord).

The non-geometric constraints can be obtained through specification on the inflow and outflow boundary conditions and the choice of the target blade pressure distributions/loading.

3.6 Inverse Design Validation

In this section, the design method is validated for inviscid and viscous flow cases ranging from subsonic to transonic regimes. The validation is carried out by analyzing the flow over two different cascade geometries and then prescribing the blade

pressure or loading distribution obtained for one of them as the target performance for the other cascade. If the inverse design method is valid, it should recover the corresponding cascade geometry and produce the prescribed pressure.

The validation cases are hypothetical geometries, which are generated using analytical camberline and thickness distributions. However these geometries can represent many features of the flow in turbomachinery cascades and are useful for assessment of the numerical scheme. For all validation cases the initial and target geometries are selected from the same family of blade profiles; i.e. they have the same axial chord and spacing, inlet and exit blade angles and similar shape of leading and trailing edges. For all these cases, the flow is subsonic at inlet and exit and the inflow and outflow boundary conditions are similar. At inflow, the total pressure, total temperature and flow angle are specified and, at outflow, the exit static pressure is specified.

3.6.1 Parabolic Cascade

The first configuration used for validation of the design scheme, is that of a parabolic cascade, where both camberline and thickness distributions assume a parabolic profile given by:

$$f(x) = \frac{1}{2}\left(\tan\beta_{out} - \tan\beta_{in}\right)x^2 + \tan\beta_{in}x \tag{3.12}$$

and

$$T(x) = 6T_{max}x(1-x) \tag{3.13}$$

where β_{in} and β_{out} are the blade inlet and exit angles, respectively, and T_{max} is the blade maximum thickness to chord ratio. This thickness distribution is symmetric around mid-chord and implies sharp LE and TE.

This configuration is used to validate the design method for viscous flow where a target pressure distribution is prescribed and for inviscid flow where a target pressure loading distribution is prescribed.

Viscous flow with $p^{\pm}$ Specified

For the first validation case, viscous flow in two different parabolic cascades is considered. The initial and target geometries have 8% and 4% maximum thickness to chord ratio, respectively. For both cases, the spacing to chord ratio is 0.5, the inlet and exit blade angles are 16° and −16°. The ratio of exit static to inlet total pressure is 0.8 and the Reynolds number is 10^6. The flow in these two cascades are first analyzed by solving the RANS equations using the same code but in analysis mode. Figure 3.5 shows the Mach contours for each configuration, where the maximum Mach numbers are 0.89 and 0.85 for the initial and target geometries, respectively. Figure 3.6 shows the streamlines near the trailing edge of the initial and target geometries. As can be seen in this figure, the flow separates at about 80% chord on the suction side of the initial geometry, whereas for the target geometry, the flow separates at about 90% chord.

The pressure distribution of the target geometry is then used as the target (prescribed) for the initial geometry. Figure 3.7 shows the initial, target and inversely computed pressure distributions on the blade surfaces and Fig. 3.8 shows the corresponding geometries. As can be seen, the computed pressure distribution along the blade surfaces agrees fairly well with the target pressure distribution and the target blade shape is also recovered accurately by the design method. Figure 3.9 shows that the L_2 norm of the blade displacement decreases more than three orders of magnitude after some 150 geometry modifications, which ensures that a steady state solution is reached at convergence. The computation time is almost

twice of that of an analysis calculation. This validation case shows that the inverse method can be used for viscous flow problems at high Reynolds numbers typical of turbomachinery flows to achieve a target pressure distribution corresponding to a realistic geometry; it also shows that this inverse method can handle design cases with mildly separated flow regions.

Inviscid Flow with Δp and ΔT Specified

The second validation case is that of an inviscid flow over two parabolic cascades with the same thickness distribution, but having different camberlines. The primary design variables are the blade pressure loading and thickness distributions rather than the pressure distributions on the blade pressure and suction sides.

For both cases, the maximum thickness to chord ratio is 5%, the spacing to chord ratio is 0.5, the inlet and exit blade angles are 10° and -10° and the ratio of exit static to inlet total pressure is 0.8. The flow in these two cascades is first analyzed by solving the Euler equations using the same code but in analysis mode. Figure 3.10 shows the Mach number contours over the initial and target geometries. The corresponding blade pressure loading and the pressure distribution along the blade surfaces are given in Fig. 3.11.

The blade pressure loading corresponding to the target geometry is then used as the target loading for the initial geometry. Figure 3.11 shows that the blade pressure loading and the pressure distribution along the blade surfaces computed by the inverse design method are in a rather good agreement with the target distributions, while Fig. 3.12 shows that the target geometry is accurately recovered by the design scheme. For this case, the design scheme converged to a solution after about 100 geometry modifications, where the L_2 norm of the blade displacement is reduced by more than two orders of magnitude, as shown in Fig. 3.13.

The time-accurate solution of the Euler equations, which is obtained after each geometry modification step, requires between 50-150 iterations in pseudo-time to converge the modified mass residual of the unsteady equations to 10^{-6}. This level of convergence was found to be sufficient for the accuracy and the stability of the design calculations. The inverse design computational time for this case is almost the twice of that taken by to analysis the same geometry.

3.6.2 Subsonic Compressor Cascade

The second configuration for validating the design scheme assumes a parabolic camberline distribution, see Eq. 3.12, while the thickness distribution assumes the following profile:

$$T(x) = \frac{3\sqrt{3}}{2} T_{max} \sqrt{x} \, (1 - x) \tag{3.14}$$

which implies round LE and sharp TE.

This configuration is used to validate the design method for inviscid flow where a target pressure distribution is prescribed and for viscous flow where a target pressure loading distribution is prescribed.

Inviscid Flow with $p\pm$ specified

For this validation case, inviscid flow over two subsonic compressor cascades is considered. The blades have significantly different camber line and thickness distribution. The maximum thickness to chord ratio is 5% and 10% and the camber line distributions assume a third and second degree profile for the initial and target geometry, respectively. The initial geometry corresponds to an aft-loaded blade whereas the target one corresponds to a mid-loaded blade. The spacing to chord

ratio is 0.75 and exit static to inlet total pressure ratio is 0.8 and the inlet and exit flow angles are 25° and −25°, respectively.

The flow in these two cascades is first analyzed using Euler equations by running the same code in analysis mode. Figure 3.14 shows the Mach contour resulting from the analysis of two geometries, where the maximum Mach number in the domain are 0.87 and 0.90 for the initial and target geometry, respectively.

The pressure distribution of the target geometry is then used as the design input. The inverse calculation starts from the initial geometry and its converged solution and reaches the target pressure distribution after about 400 modifications of the initial geometry. Figures 3.15 and 3.16 gives a comparison of initial, target and inversely computed pressure distributions and corresponding geometries. The agreement between target and computed geometries is rather excellent and the target pressure distribution is also reached at convergence. Figure 3.17 shows that the mesh velocities L_2 norm has decreased by more than two orders of magnitude during the design calculation. The computational time of the inverse design calculation is almost twice that an analysis calculation of the same geometry with the same mesh.

This case shows the robustness of the scheme to recover a geometry corresponding to a target pressure distribution which is significantly different from that corresponding to the initial geometry; this case provides a good assessment of the design scheme for large deformation of the computational domain through the design process. It also shows that the LE/TE treatment is capable of recovering the target geometry in those regions as long as the initial and target geometries are from the same family of blade shape.

Viscous Flow with Δp and ΔT Specified

The second validation case is that of viscous flow in two subsonic compressor cascade where the pressure loading and thickness distributions are prescribed. The initial and target blade profiles assume the same thickness distribution, while the camberline distributions are generated by third and second degree polynomials, respectively. The maximum thickness to chord ratio is 5%, the spacing to chord ratio is 0.5 and the inlet and exit flow angles are 25° and $-10°$, respectively.

The viscous flow in the initial and target geometries are first analyzed using RANS equations by running the same code but in analysis mode. Figure 3.18 shows the Mach number contours resulting from the analysis of each case. Further inspection of the flow field reveals that there are regions of slightly separated flow near the trailing edge for both cases, which are clearly shown in Fig. 3.19. The pressure loading and the pressure distribution on the blade resulting from the analysis of the original and target geometry, which are given in Fig. 3.20, show that the initial geometry has a negative loading distribution between 0 and 35% chord, while the target loading has a positive loading on the whole blade. Let us note that the initial geometry is not a realistic one because of the reverse loading, however it is used here to demonstrate the robustness and ability of the method in handling large geometry changes as well as mildly separated flow regions.

The design scheme is applied to this case to achieve the target loading distribution and recover the target blade geometry. The resulting blade loading and pressure distribution along the blade obtained from the inverse design method show a good agreement with the target distributions and the target blade geometry has also been recovered fairly well, as shown in Fig. 3.21. The computed blade geometry has been obtained after 200 modifications of the initial geometry. The design

computations require about twice the time required to analyze the same geometry. Figure 3.22 shows the convergence of the L_2 norm of the mesh displacement, which ensures that a steady-state solution is reached on the latest geometry. This validation case shows that the design scheme can be applied to viscous and turbulent flow with mild separation regions and can handle large deformation of the computational domain through the design process.

3.6.3 Impulse Turbine Cascade

This validation case is that of an inviscid flow over transonic impulse turbine cascades, where the blade camberline and thickness distribution assume a parabolic distribution. The initial and target blade shapes are similar except for the maximum thickness to chord ratio T_{max}, which differs by 3% chord. The inlet and exit blade angles are $-40.30°$ and $40.30°$, the spacing to chord ratio is 0.526 and the exit static to inlet total pressure ratio is 0.833. The initial and target geometries are first analyzed by solving Euler equations using the same code but in analysis mode. Figure 3.23 shows the Mach contours resulting from the flow analysis of the initial and target geometries, where a shock occurs around 60% chord on the suction side of the original geometry. Although the initial and target geometries are very similar, the resulting flow fields are clearly distinctive, where the corresponding maximum Mach numbers are 1.5 and 1.0, respectively.

For the design calculations, the pressure distribution of the thinner cascade surfaces ($18.5\%T_{max}$) is used as the prescribed (target) design input and the design scheme is executed starting from a converged solution on the original geometry ($21.5\%T_{max}$). Figure 3.24 shows the initial, target and inversely computed pressure distributions, whereas Fig. 3.25 shows the corresponding geometries. The

design technique accurately reproduces the target geometry as well as the target pressure distributions on the blade pressure and suction surfaces. The target geometry is reached after some 300 geometry modifications of the initial geometry. The L_2 norm of the blade displacement is given in Fig. 3.26. For this case, the inverse design computation time is almost the twice that of one analysis calculation. Numerical experiments with this case suggest that a higher relaxation factor and more smoothing of the blade shape are needed to obtain a converged solution. This example shows the usefulness of the scheme to handle/control shock waves in the transonic flow regime.

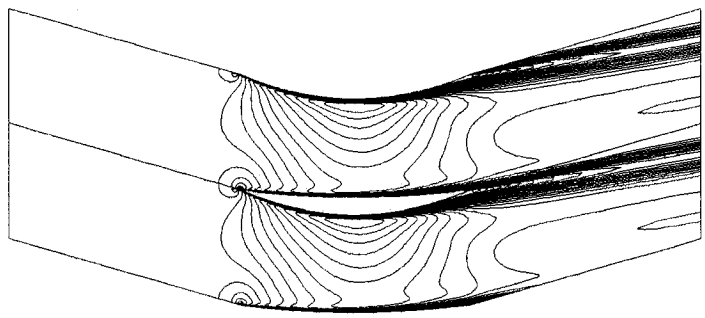

(a)

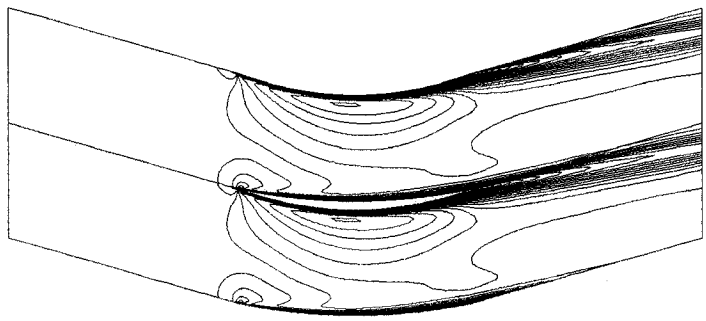

(b)

Figure 3.5: Mach contour field for viscous flow in parabolic cascades (a) Initial blade $T_{max}/c = 8\%$ and (b) Target blade $T_{max}/c = 4\%$

(a) (b)

Figure 3.6: Streamlines near trailing edge of parabolic cascade
(a)Initial blade (b) Target blade

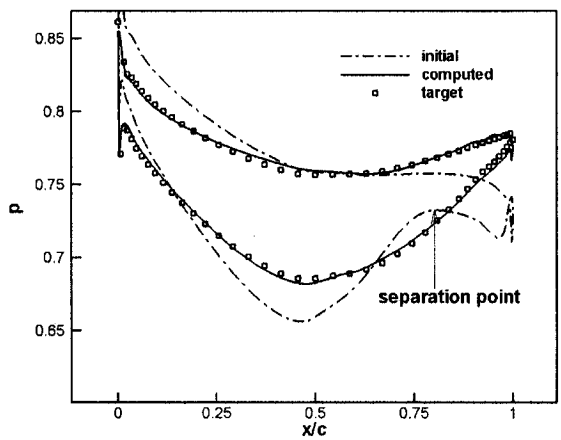

Figure 3.7: Pressure distributions for viscous flow in parabolic cascades

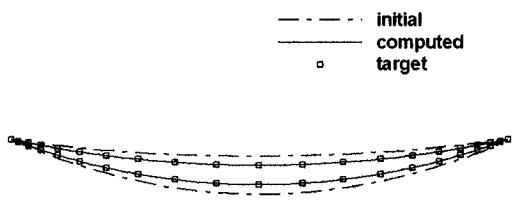

Figure 3.8: Initial, target and design geometry of parabolic cascade

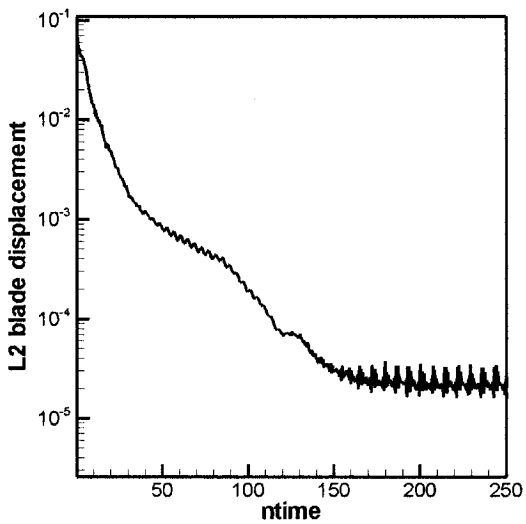

Figure 3.9: Convergence history of parabolic cascade design calculation

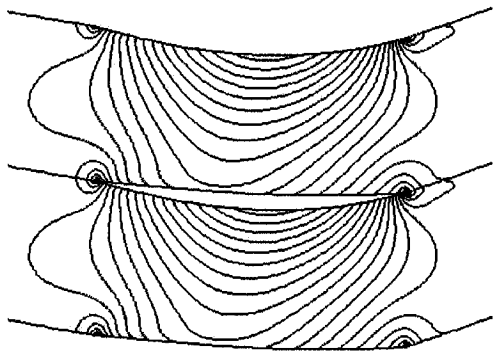

(a)

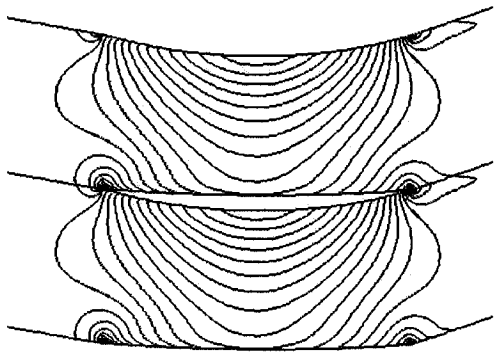

(b)

Figure 3.10: Mach contour field for inviscid flow in parabolic cascades (a) Initial blade $T_{max}/c = 5\%$ and (b) Target blade $T_{max}/c = 5\%$

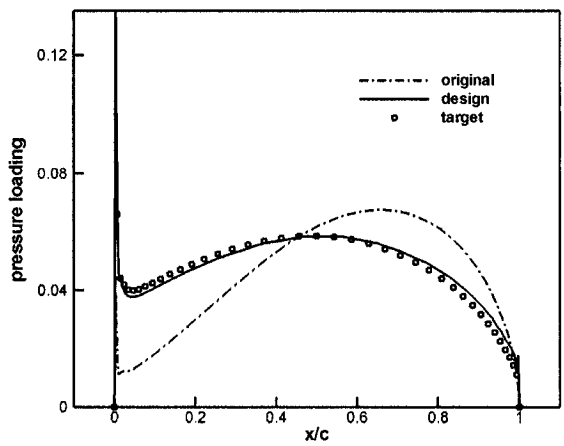

(a)

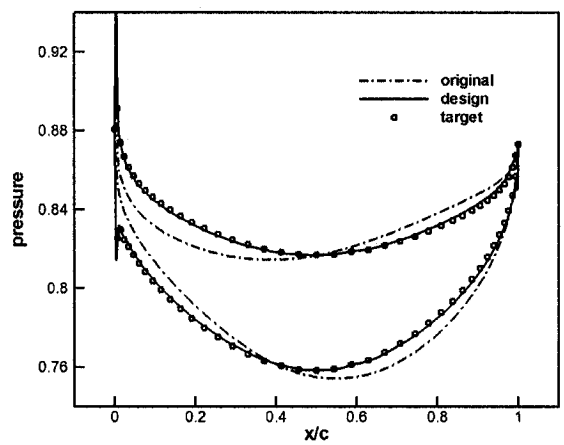

(b)

Figure 3.11: Pressure loading and pressure distributions for parabolic cascades

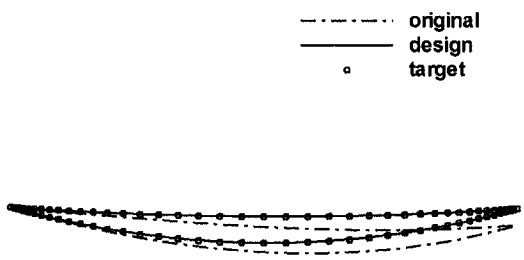

Figure 3.12: Initial, target and design geometry of the parabolic cascades

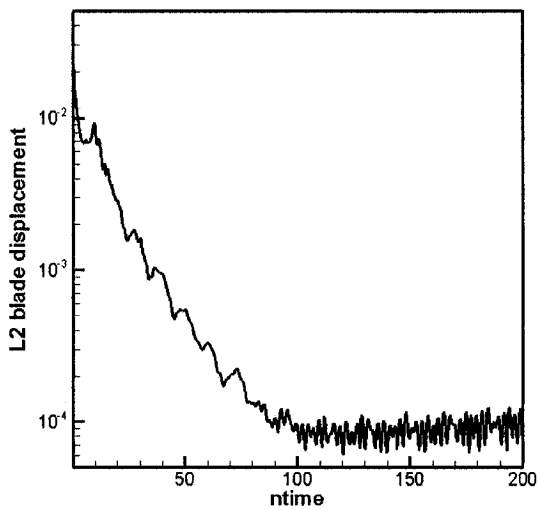

Figure 3.13: Convergence history of parabolic cascade design calculation

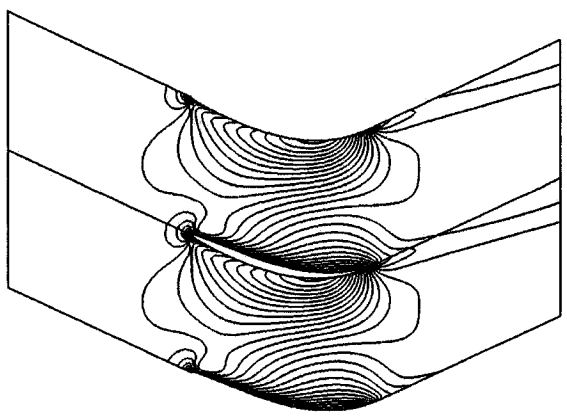

(a)

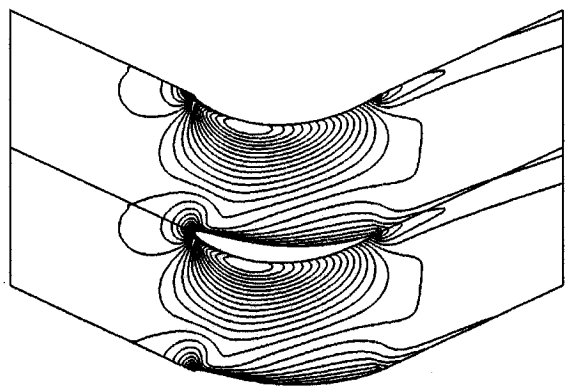

(b)

Figure 3.14: Mach contour field for inviscid flow in subsonic compressor cascades (a) Initial blade $T_{max}/c = 5\%$ and (b) Target blade $T_{max}/c = 10\%$

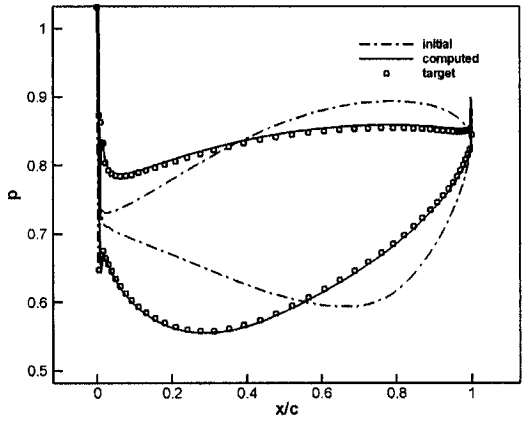

Figure 3.15: Pressure distributions for subsonic compressor cascades

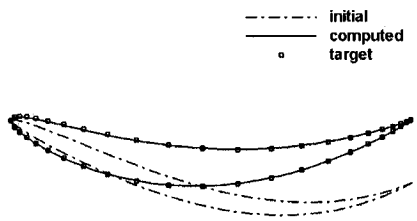

Figure 3.16: Initial, target and design geometries of subsonic compressor cascade

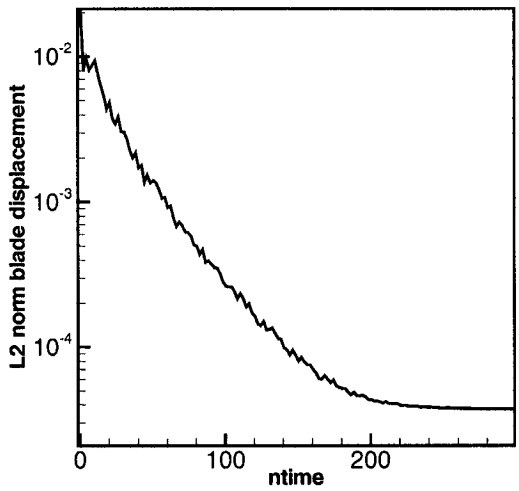

Figure 3.17: Convergence history of compressor cascade design calculation

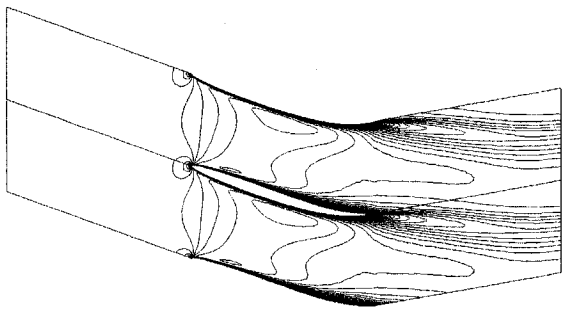

(a)

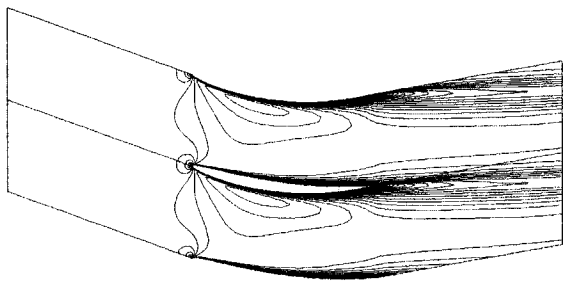

(b)

Figure 3.18: Mach contour field for viscous flow in subsonic compressor cascades (a) Initial blade $T_{max}/c = 5\%$ and (b) Target blade $T_{max}/c = 5\%$

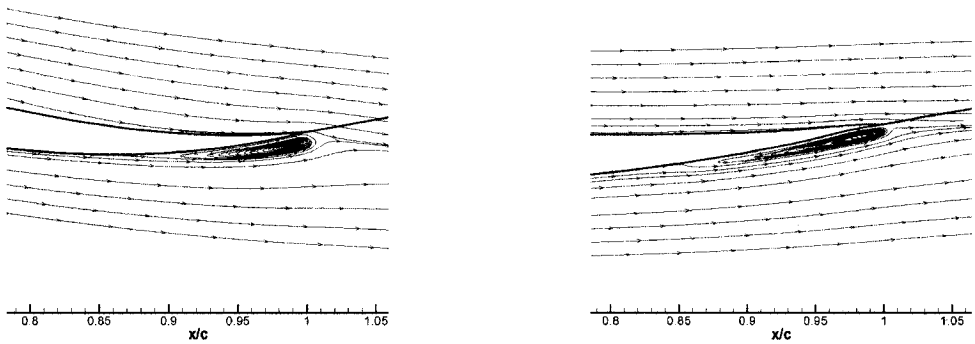

(a) (b)

Figure 3.19: Stream lines near the trailing edge of subsonic compressor cascades (a) Initial blade and (b) Target blade

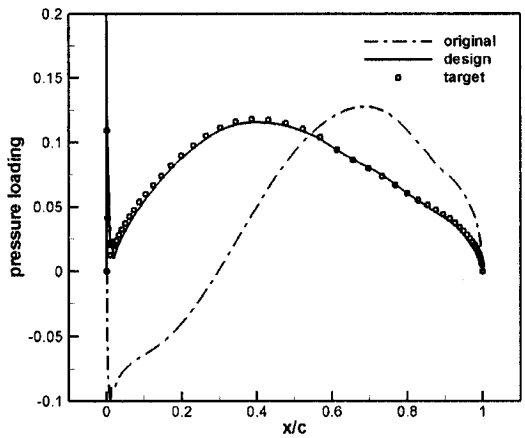

(a)

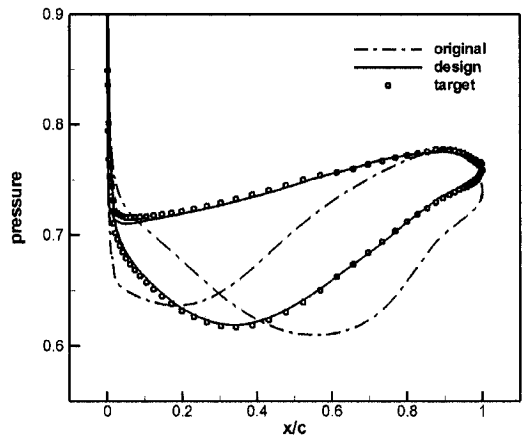

(b)

Figure 3.20: Pressure loading and pressure distributions for compressor cascades

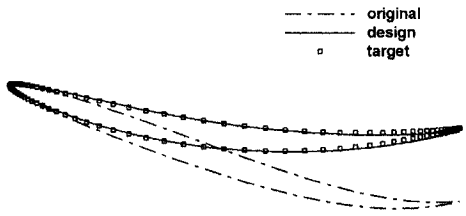

Figure 3.21: Original, target and design geometry of the compressor cascades

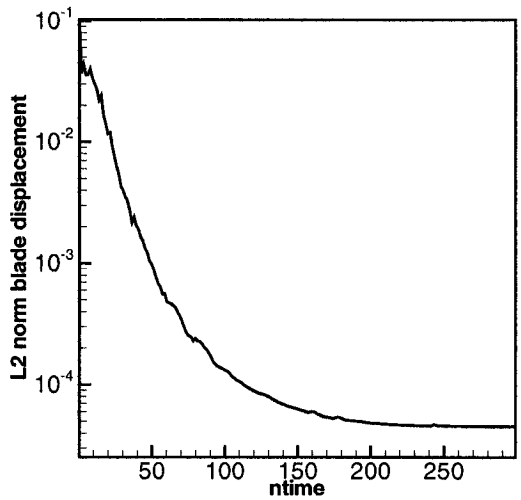

Figure 3.22: Convergence history of compressor cascade design calculation

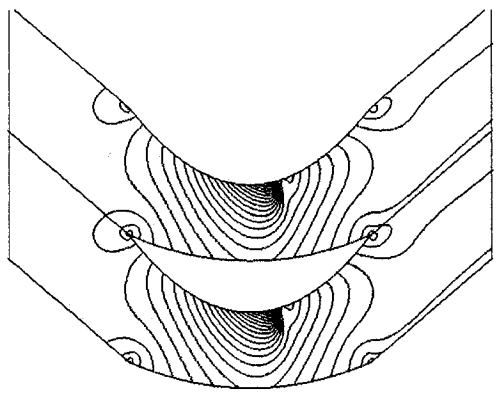

(a)

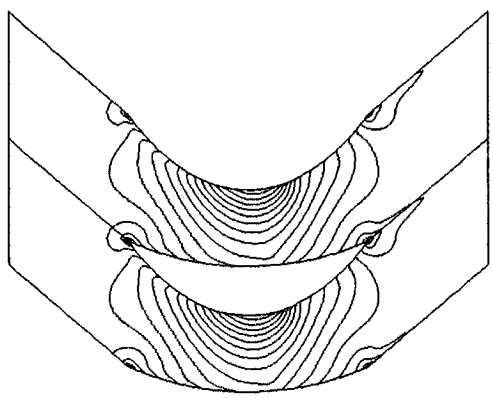

(b)

Figure 3.23: Mach contour field for inviscid flow in transonic compressor cascades (a) Initial blade $T_{max}/c = 21.5\%$ and (b) Target blade $T_{max}/c = 18.5\%$

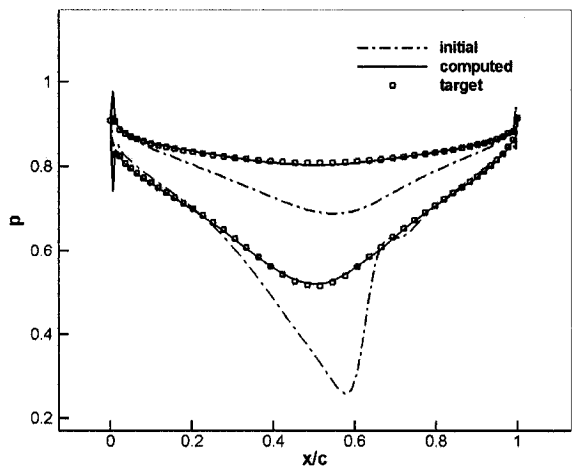

Figure 3.24: Pressure distributions for transonic impulse cascades

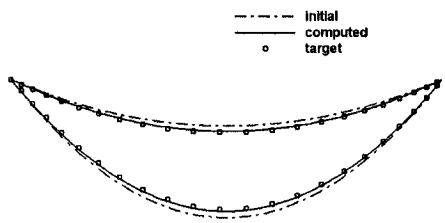

Figure 3.25: Initial, target and design blade profiles of impulse cascades

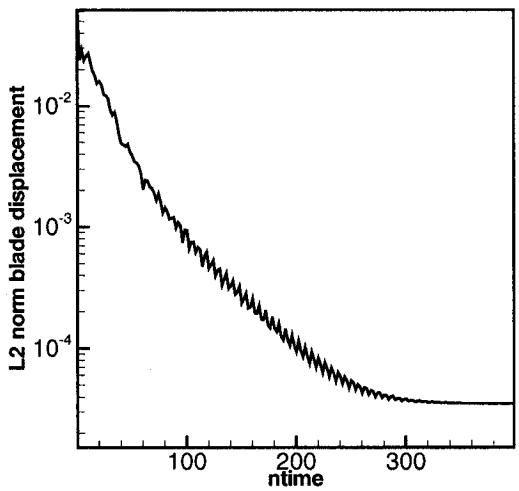

Figure 3.26: Convergence history of impulse cascade design calculation

Chapter 4

Application to Modern Gas Turbine Blades

In this chapter the inverse design method is applied to compressor and turbine blades typical of those used in modern gas turbine engines. The usefulness and flexibility of the inverse method is demonstrated on the successful design of a number of compressor and turbine blade cascades ranging from subsonic to transonic flow. The prescribed design quantities assume a smooth distribution, which eliminates sudden expansion or diffusion of the flow so as to remove/weaken shock waves in transonic flow regime and/or reduce separation regions. In cases where a solution does not exist for the prescribed design quantities, the inverse design scheme produces a smooth blade shape that would give a close approximation of the target performance.

4.1 ONERA Transonic Compressor Cascade

The first design case is a highly loaded transonic compressor cascade that was tested at ONERA [16]. This compressor cascade has been designed using a target pressure

distribution to remove/weaken the passage shock. The inlet flow angle is 30° and the flow turning is almost 50°. This cascade is first analyzed using RANS equations. For the flow analysis the exit static pressure is 0.733 and the Reynolds number is $Re = 1.5 \times 10^6$. For the design calculations, the inflow boundary conditions are reduced mass flow rate, total temperature and flow angle, while the static pressure is specified at the outflow boundary.

The resulting Mach number field, given in Fig. 4.1(a), shows the presence of a detached shock that impinges on the suction side where the maximum Mach number is around 1.34. The flow separates due to shock-boundary layer interaction on the suction side but reattaches again and remains attached on the rest of the blade. The corresponding pressure distribution on the blade surfaces is given in Fig. 4.2. This cascade is then designed to achieve a smoother pressure distribution, which is also shown in Fig. 4.2, so as to remove the detached shock wave. The total blade loading (which is equal to the difference in prescribed pressure on the blade surfaces, $p^+ - p^-$) was increased by less than 1%, therefore the resulting blade shape is expected to have almost the same global flow turning and the same tangential force as the original blade. As mentioned earlier, the reduced mass flow rate, which can be chosen as an input to the CFD simulation, is the same for both original and designed blades.

The designed cascade is transonic shock-free with a maximum Mach number of 1.2, as can be seen form the Mach contour field given in Fig. 4.1(b). Figure 4.3 shows a comparison of the original and design blade profiles. The inverse design solution is obtained after some 75 geometry modifications. The computation time taken by the inverse method is less than the time taken to analyze the flow over the same geometry. This is due to the relatively small number of geometry modification, which was required to achieve the target pressure distribution. A comparison of target

and inversely computed pressure distributions shows a good agreement between the target and the inversely computed pressure distributions. The results also indicate that the pressure loss of the designed blade has been decreased about 20%, which can be attributed to the shock wave removal. The cascade static pressure ratio has also increased by 3%. Let us note that these improvements in aerodynamic performance are not directly controlled in the inverse design, they are rather implications of prescribing a "good" pressure distribution.

4.2 DFVLR-T106 Subsonic Turbine Cascade

The case presented in this section is that of a blade cascade with a shape similar to a subsonic turbine rotor blade that was tested at DFVLR [16]. For the original blade, the flow inlet angle is 37.7°, and the flow turning is about 90°, the exit static pressure is 0.789 and the Reynolds number is 5.10^5. The inflow and outflow boundary conditions, namely, inlet the total pressure, total temperature, flow angle, and exit static pressure are given from experimental data and are kept the same for the original and the designed blades.

For the original blade, the Mach contour field and the corresponding pressure distribution on the blade surfaces are given in Figs. 4.4(a) and 4.5. Figure 4.5 shows a rapid flow acceleration followed by high diffusion between 30% to 80% chord on the blade suction side. This cascade is designed to achieve a smoother pressure distribution on the suction side, keeping the same distribution on the pressure side, see Fig. 4.5. The blade total loading was increased by less than 0.5%. Note that it is possible to keep exactly the same total loading, as it is directly controlled by the prescribed pressure distributions.

A comparison of the target and design pressure distributions, given in Fig.

4.5, shows that the computed pressure distribution using the inverse method is in good agreement with the target. A comparison of the original and designed blade profiles is given in Fig. 4.6. The designed blade is obtained after almost 120 geometry modifications, which translates to a computational time similar to an analysis calculation of the same geometry with the same mesh. The Mach contour field for the the designed blade is also shown in Fig. 4.4(b), where the maximum Mach number is 0.662. The total pressure loss of the designed blade has decreased by 14% compared to the original blade, while there is a 1.2% reduction of the reduced mass flow rate. We note again that these are implications of prescribing the target pressure distribution and are not directly controlled by the inverse method.

4.3 NACA Transonic Compressor Cascade

The case presented in this section is a NACA transonic compressor cascade [56]. For the original blade, the flow inlet angle is 59.9° and the flow turning is less than 10.0°. The resulting flow field, presented in Fig. 4.7(a), shows the presence of a bow shock that impinges on the blade suction side at about 45% chord and results in boundary layer separation at this location. The flow remains separated on the rest of the blade suction side, as it can be seen by the flow stream lines, plotted in Fig. 4.8(a).

This cascade is then designed to achieve a target pressure loading distribution while keeping the same thickness distribution as the original blade. The original and target total pressure loading assume the same value. The target pressure loading distribution is obtained by averaging the original loading distribution with a parabolic one, with the same total loading. The resulting target loading also has the same characteristics near the blade leading and trailing edges, which is important

for a realistic target pressure loading distribution. The shock strength is expected to be weaker and the loading be more uniformly distributed over the designed blade. Since the flow is well-behaved on the blade pressure side, p^+ calculated from the time-accurate solution and the prescribed loading were used to update p^-, as given in Eqs. 3.3.

Given that this is a transonic flow case, the reduced mass flow rate computed for the original blade is imposed as inflow boundary condition for the designed blade, other boundary conditions being the same. The design solution satisfies the target loading distribution fairly well, after about 250 geometry modifications, see Fig. 4.9(a). The corresponding pressure distributions are also shown in Fig. 4.9(b), where a good agreement between the target and the design distributions is obtained. The computation time is almost three times that of an analysis calculation. The flow field over the designed blade is presented in Fig. 4.7(b); the resulting stream lines, shown in Fig. 4.8(b), indicate that the separation region has decreased from 50% to 10% chord, which is quite significant. The static pressure ratio of the cascade has also increased by 10% and the total pressure loss has decreased by 15%.

Let us note again that the reduction of the separation region, as well as the improvements in the blade aerodynamic performance, are implications of imposing the target loading distribution, therefore an experienced designer can take advantage of this method. Figure 4.10 shows a comparison of the original and the designed blade profiles. The designed blade has an S-shape configuration, which has also been observed by other researchers, in order to weaken the shock strength. It was found that this choice of target pressure loading prevents shock-boundary layer separation, as shown in Fig. 4.8.

This case shows that the design scheme can be effectively used for designing blades in transonic flow regime in the presence of shock waves and relatively large

(but bounded) separation regions.

4.4 VKI-LS89 Transonic Turbine Cascade

This case is that of a high pressure transonic turbine nozzle guide vane profile, tested at the von Karman Institute [57]. The flow enters the blade axially and undergoes a flow turning of about 80°. The spacing to chord ratio is 0.85. The Reynolds number is 1.26×10^6 and exit isentropic Mach number M_{2is} is 0.875, which corresponds to an exit back pressure ratio of about 0.6. The resulting Mach number field is presented in Fig. 4.11(a), where the maximum Mach number is 1.14. The corresponding pressure distribution for the original blade is given in Fig. 4.12.

A target pressure distribution is then constructed by smoothing the pressure distribution on the blade suction side. The smoothed pressure distribution results in a 5% increase in the blade total loading.

Figure 4.12 shows that the pressure distribution obtained on the designed profile agrees fairly well with the target pressure distribution. The designed blade shape is obtained after 100 geometry modifications, which requires a computational time similar to an analysis of the same geometry. Figure 4.11(b) shows the Mach number field on the designed geometry, where the maximum Mach number in the flow field is 1.12. Figure 4.13 shows a comparison of the original and designed blade profiles. The results show that the total pressure loss is reduced by 8% as an indirect result of imposing a smoother target pressure distribution, while there is 2.8% reduction in the reduced mass flow rate.

(a)

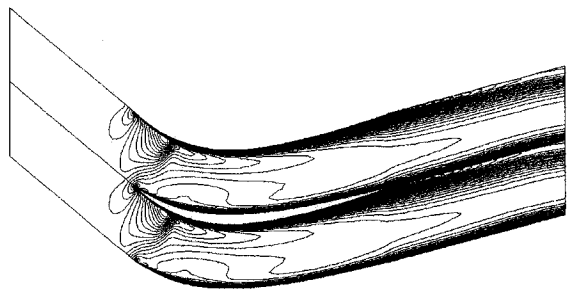

(b)

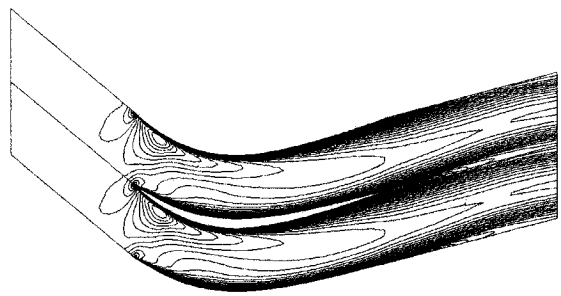

Figure 4.1: Mach contours for the ONERA compressor cascade (a)original blade $M_{max} = 1.34$, (b)designed blade $M_{max} = 1.20$

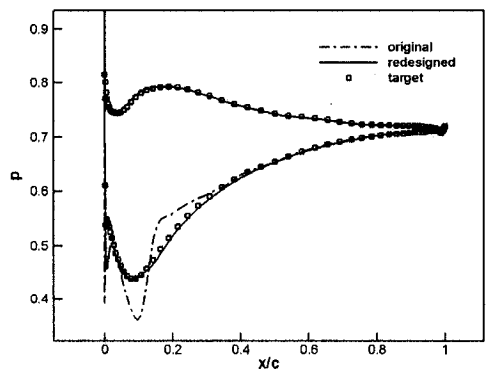

Figure 4.2: Pressure distributions for ONERA compressor cascade

Figure 4.3: Original and designed geometries of ONERA compressor cascade.

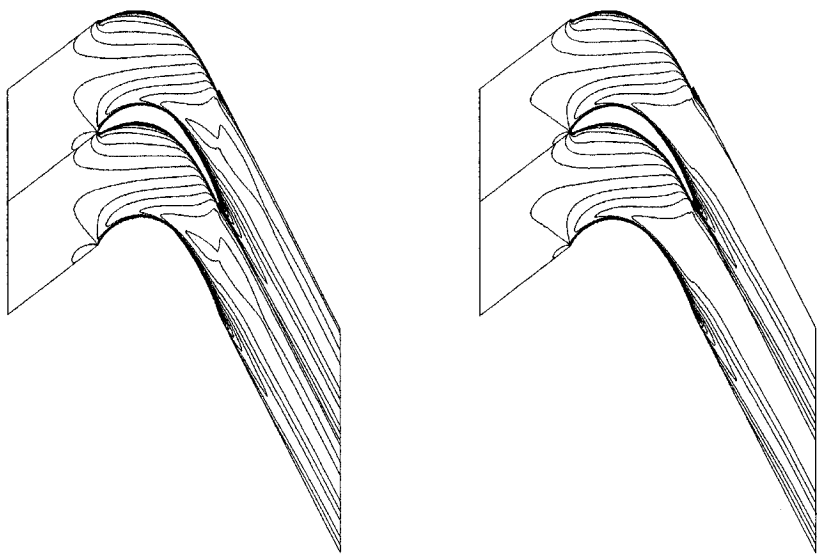

Figure 4.4: Mach contours for DFVLR turbine cascade
(a)original blade $M_{max} = 0.68$, (b)designed blade $M_{max} = 0.66$

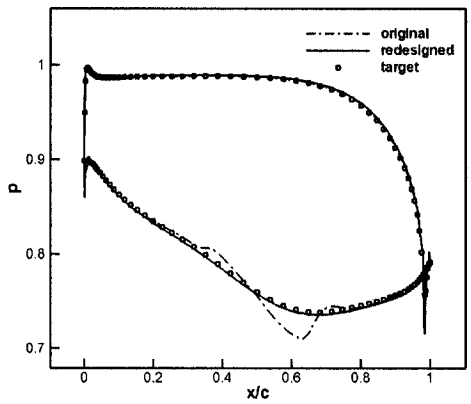

Figure 4.5: Pressure distributions for DFVLR cascade

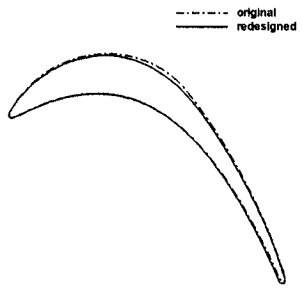

Figure 4.6: Original and design geometry of the DFVLR turbine cascade.

(a) (b)

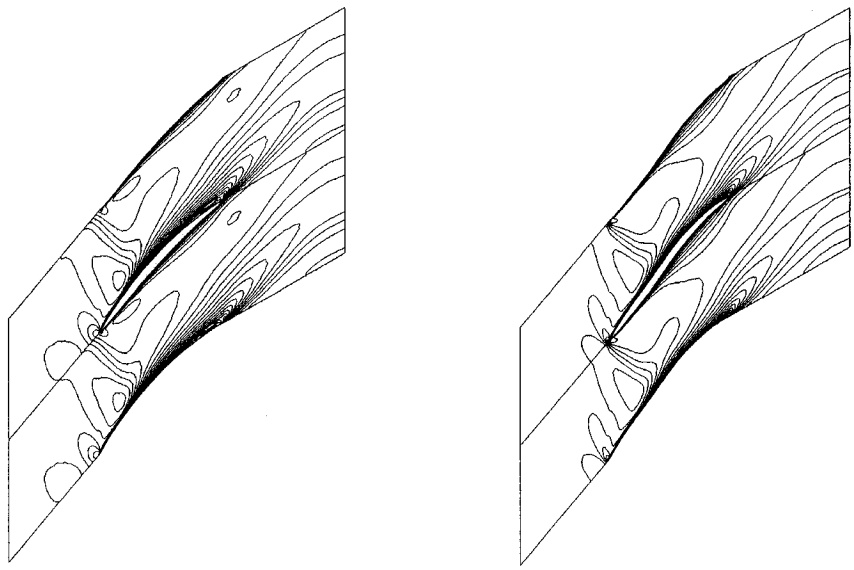

Figure 4.7: Mach contours for NACA compressor cascade
(a)original blade $M_{max} = 1.2$, (b)designed blade $M_{max} = 1.2$

(a) (b)

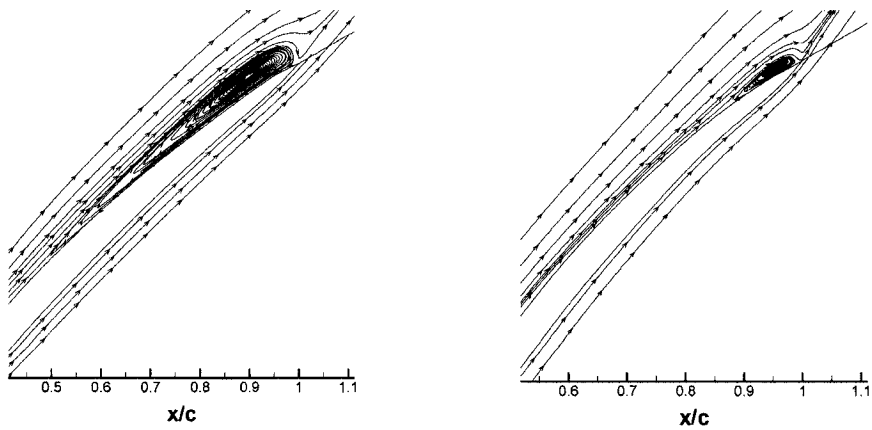

Figure 4.8: Stream lines for NACA compressor cascade.
(a)original blade, (b)designed blade

(a)

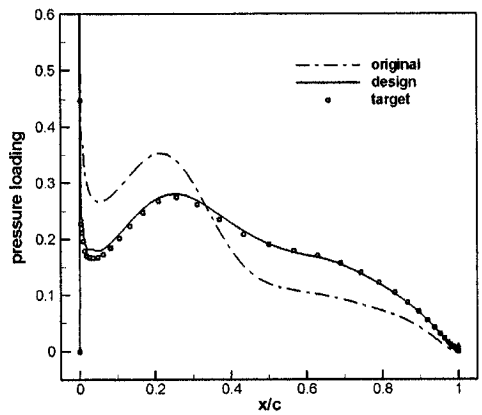

(b)

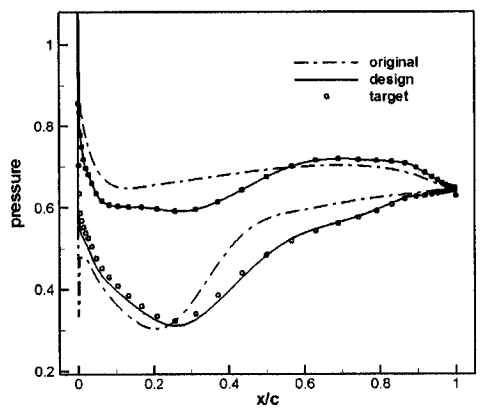

Figure 4.9: Loading and pressure distributions for NACA compressor cascade

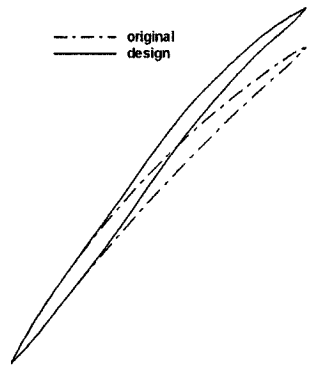

Figure 4.10: Original and design geometry of NACA compressor cascade

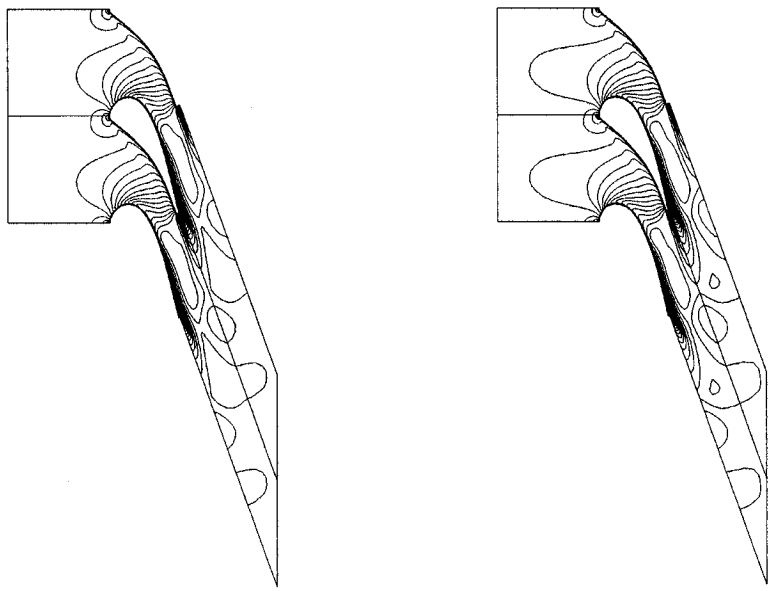

Figure 4.11: Mach contours for VKI turbine cascade
(a)original blade $M_{max} = 1.14$, (b)designed blade $M_{max} = 1.12$

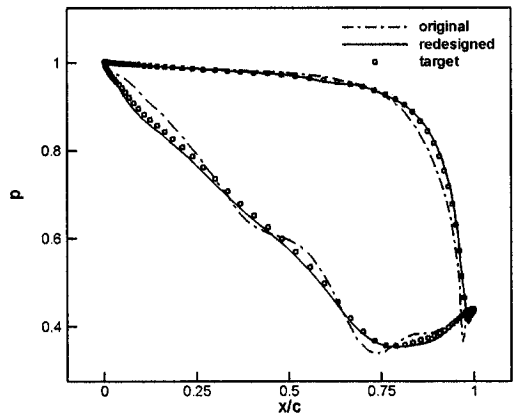

Figure 4.12: Pressure distributions for VKI turbine cascade

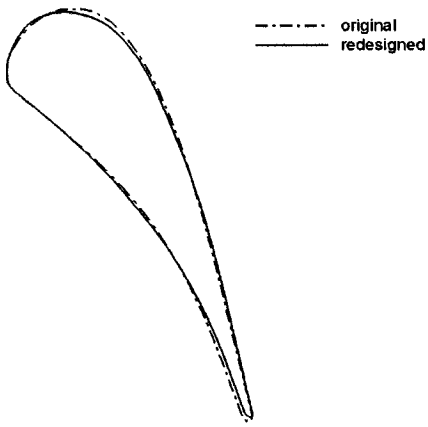

Figure 4.13: Original and designed geometry of VKI cascade

Chapter 5

Conclusion and Recommendations

5.1 Summary

A new aerodynamic inverse shape design method, applicable to 2D and 3D compressible viscous flow in turbomachinery blading, has been developed, validated and applied to design linear cascades in 2D turbulent flow in the subsonic and transonic flow regimes. The design variables are either the pressure distribution on the blade suction and pressure surfaces or the blades pressure loading and their thickness distribution. Starting from an initial guess for the blades profile, they are iteratively reshaped by moving their surfaces at a virtual velocity that would make the momentum flux on the blades equal to the flux that would result from the prescribed pressure distribution. Since the flow is inherently unsteady due to the blade movement, the inverse method is implemented in a consistent manner into the unsteady RANS equations that are solved on a moving mesh using an ALE formulation. The method is first validated for inviscid and viscous flows in cascades. The validation results indicate that the method is rather robust and capable of recovering the target geometry and performance. The usefulness of the inverse method in reshaping the

blades to accomplish a given pressure loading distribution is then demonstrated on the successful design of transonic compressor cascades to remove/weaken the shock, and the design of a subsonic and a transonic turbine blade to achieve a smoother pressure distribution. The results also show that the inverse design method is capable of handling relatively large (but bounded) separated flow regions and can be effectively used to reduce such regions. The results also showed that an experienced designer can indirectly improve the blade performance by properly tailoring the target pressure distribution or loading.

5.2 Future Work

There are several possible extensions to the present work. Some have to do with the CFD code development and some have to do with the design methodology and implementation. Some examples are given below.

1. An important feature of this inverse formulation is the possible extension to 3D flow fields. This extension is probably the primary goal of future research, and is based on the full 3D RANS or Euler equations, where the virtual velocity assumes the form $\mathbf{v}_v^{\pm} = (u_v^{\pm}, v_v^{\pm}, w_v^{\pm})$.

2. For the cases, where the blade thickness distribution is prescribed as a design input, a tangential thickness distribution (in y-direction) is used to construct the blade geometry. In cases where the blades are highly staggered, formulation of the inverse method in terms of normal thickness distribution would be advantageous [46].

3. As for CFD development, extension of the code for 3D flow fields is desirable. A higher order turbulence model, such as $(K-\epsilon)$ model, is recommended for 3D flow since identification of turbulence stations required for algebraic turbulence models

for unstructured grids becomes a cumbersome task in 3D flows.

Bibliography

[1] Pierret, S., Demeulenaere, A., Gouverneur, B., Hirsch, C., and Van den Braembussche, R. (2000) Designing turbomachinery blades with the function approximation concept and the navier-stokes equations. *AIAA paper 2000-4879.*

[2] Nemec, M. and Zingg, D. (2001) Towards efficient shape optimization based on navier-stokes equations. *AIAA paper 2001-2532.*

[3] Mengistu, T. and Ghaly, W. (2004) Single and multipoint shape optimization of gas turbine blade cascades. *AIAA paper 2004-4446.*

[4] Lakshminarayana, B. (1996) *Fluid Dynamics and Heat Transfer of Turbomachinery*. New York, John Wiley & Sons.

[5] Rai, M. (1987) Unsteady 3d navier-stokes simulation of turbine rotor-stator interaction. *AIAA Paper 87-2038.*

[6] Dawes, W. (1992) Towars improved throughflow capability: The use of three-dimensional viscous flow solver in a multi-stage invironment. *Journal of Turbomachinery*, **114**, 8–17.

[7] Arnone, A. and Pacciani, R. (1993) Rotor-stator interaction analysis using the navier-stokes equations and a multigrid method. *Journal of Turbomachinery*, **118**, 605–614.

[8] SBonaiuti, D., Arnone, A., Milani, A., and Baldassarre, L. (2003) Aerodynamic analysis of a multistage centrifugal compressor. *ASME Paper GT-2003-38495*.

[9] Hirt, C., Amsden, A., , and Cook, J. (1974) An arbitrary lagrangian-eulerian computing method for all flow speeds. *Journal of Computational Physics*, **14**.

[10] Pracht, W. Caculating three-dimensional fluid flows at all speeds with an eulerian-lagrangian computing mesh. *Journal of Computational Physics*.

[11] Sadeghi, M. and Liu, F. (2001) Computation of mistuning effects of cascade flutter. *AIAA Journal*, **39(1)**, 22–28.

[12] Cinnella, P., De Palma, P., Pascazio, G., and Napolitano, M. (2004) A numerical method for turbomachiney aeroelasticity. *Journal of Turbomachinery*, **126**, 310–316.

[13] Kielb, R. and Barter, J. (2004) Expeimental and numerical study of stall flutter in a transonic low-aspect ratio blisk. *Journal of Turbomachinery*, **126**, 166–174.

[14] Clark, S. and Hall, C. (2000) A time-linearized navier-stokes analysis of stall flutter. *Journal of Turbomachinery*, **122**, 467–476.

[15] Bladh, R. and Pierre, C. (2002) Dynamic response predictions for a mistuned industrial turbomachinery rotor using reduced-order modelling. *Journal of Turbomachinery*, **124**, 311–323.

[16] Fottner, L. (1990) Test cases for computation of internal flows in aero engine components. *AGARD-AR-275*.

[17] Chima, R. and Johnson, G. (1985) Effiicient solution of the euler and navier-stokes equations with a vectorized multiple grid algorithm. *AIAA Journal*, **23(1)**, 23–32.

[18] Davis, R., Ni, R., and Carter, J. (1985) Cascade viscous flow analysis using navier-stokes equation. *AIAA Journal*, **23(10)**, 1156–1563.

[19] A., A. and R.C., S. (1993) A navier-stokes solver for turbomachinery applications. *Journal of Turbomachinery*, **115**, 305–313.

[20] Ahmadi, M. and Ghaly, W. (1998(3)) A finite volume method for inviscid transonic cascade flow with solution adaptation on unstructured mesh. *CASI Journal*, **44**, 175–181.

[21] Dawes, W. (1988) Development of a three-dimensional navier-stokes solver for application to all types of turbomachinery. *ASME Paper 88-GT-70*.

[22] Arnone, A., Liou, M., and Povinelli, L. (1993) Multigrid calculation of three-dimensional viscous cascade flows. *Journal of Propulsion and Power*, **9(4)**, 605–614.

[23] Sayma, A., Vahdati, M., and Sbardella, L. (2000) Modeling of 3d viscous compressible turbomachinery flows using unstructured hybrid grids. *AIAA Journal*, **38**, 945–954.

[24] Liu, F. and Jameson, A. (1993) Cascade flow calculations by a multi-grid euler method. *AIAA Journal of Propulsion and Power*, **9(1)**, 90–97.

[25] Holmes, D. and Connel, S. (1989) Solution of 2-d navier-stokes equations on unstructured adaptive meshes. *AIAA paper no. 81-1259*.

[26] Martinelli, L. (1987) *Calculation of Viscous Flows with a Multigrid Method*. Ph.D. thesis, Princeton University, Department of Machanical and Aerospace Engineering.

[27] Ahmadi, M. (1998) *Aerodynamic Inverse Design of Turbomachinery Cascades.* Ph.D. thesis, Concordia University, Department of Machanical and Industrial Engineering.

[28] Jameson, A., Schmidt, W., and E., T. (1981) Numerical solution of the euler equation by finite-volume methods using runge-kutta time stepping schemes. *AIAA paper no. 81-1259.*

[29] Giles, M. (1990) Nonreflecting boundary conditions for euler equation calculations. *AIAA Journal*, **28(12)**.

[30] Baldwin, B. and Lomax, H. (1978) Thin layer approximation and algebraic model for separated turbulent flows. *AIAA paper 78-257.*

[31] Jameson, A. (1991) Time dependent calculations using multigrid, with application to unsteady flow past airfoils and wings. *AIAA paper 91-1596.*

[32] Barth, T. (1990) Numerical aspects of computing high reynolds number flows on unstructured meshes. *AIAA Paper 91-0721.*

[33] Mavripilis, D. (1995) Three-dimensional mutli-grid reynolds averaged navier-stokes solver for unstructured meshes. *AIAA Journal*, **3**, 445–453.

[34] Arnone, A. and Pacciani, R. (1995) Rotor-stator interaction analysis using the navier-stokes equations and a multigrid method. *ASME paper 95-GT-177.*

[35] Dang, T. (1995) Inverse method for turbomachinery blade using shock-capturing techniques. *AIAA paper no-95-2465*, pp. 2050–2058.

[36] Lighthill, M. (1945) A new method of two-dimensional aerodynamic design. *Aeronautical Research Council R & M 2112.*

[37] Sanz, J. (1988) Automated design of controlled diffusion blades. *ASME paper 88-GT-139*.

[38] Leonard, O. and Van den Braembussche, R. (1992) Design method for subsonic and transonic cascades with the prescribed mach number distribution. *Transaction ASME*, **114(3)**, 553–560.

[39] Demeulenaere, A. and Van den Braembussche, R. (1996) Three dimensional inverse method for turbomachinery blading design. *ASME paper 96-GT-039*.

[40] Demeulenaere, A., Leonard, O., and Van den Braembussche, R. (1998) Three-dimensional inverse method for turbomachinery blading design. *Journal of Turbomachinery*, **120**, 247–255.

[41] Demeulenaere, A., Leonard, O., and Van den Braembussche, R. (1997) A two-dimensional navier-stokes inverse solver for compressor and turbine blade dasign. *Proc. Inst. Mech. Eng. PART A.*, **211**, 299–307.

[42] de Vito, L., den Braembussche, V., and R., H., Deconinck (2003) A novel two-dimensional viscous inverse design method for turbomachinery blading. *Journal of Turbomachinery*, **125**, 310–316.

[43] Hawthorne, W., Tan, C., Wang, C., and Mc Cune, J. (1984) Theory of blade design for large deflection, part i : two-dimensional cascades. *Journal of Engineering for Gas Turbines and Power*, **106(2)**, 346–353.

[44] Dang, T. and Isgro, V. (1995) Euler-based inverse method for turbomachinery blades: Part 1- two dimensional cascades. *AIAA Journal*, **33(12)**, 2309–2315.

[45] Dang, T., Damle, S., and Qui, X. (2000) Euler-based inverse methods for turbomachinery blades: Part 2- three dimensions. *AIAA Journal*, **38(11)**, 2307–2013.

[46] Medd, A. (2002) *Enhanced Inverse Design Code and Development of Design Strategies for Transonic Compressor Blading*. Ph.D. thesis, Syracuse University, Department of Machanical and Aerospace Engineering.

[47] Medd, D. T., A.J. and Larosiliere, L. (2003) 3d inverse design loading strategy for transonic axial compressor blading. *ASME paper no. 2003-GT-38501*.

[48] Zangeneh, M. (1994) Inviscid-viscous interaction metod for 3d inverse design of centrifugal impellers. *Journal of Turbomachinery*, **116**, 280–290.

[49] Tong, S. and Thompkins, W. (1982) Inverse or design calculation for nonpotential flows in turbomachinery cascades. *ASME paper 82-GT-220*.

[50] Thompkins, W. and Tong, S. (1982) A design calculation procedure for shock-free or strong passage shock turbomachinery cascades. *Journal of Engineering for Power*, **106**, 281–285.

[51] Yang, T. and Ntone, F. (1986) Viscous compressible flow direct and inverse computation with illustration. *NASA-CR-175037*.

[52] Hall, E., Topp, D., Heidegger, N., McNulty, G., Weber, K., and Delaney, R. (1996) Investigation of advanced conterrotation blade configuration concepts for high speeds turboprob systems: Task vii - endwall treatment inlet flow distortion analysis final report. *NASA CR-195468*.

[53] Hathaway, M. and Wood, J. (1997) Application of a multi-block cfd code to investigate the impact of geometry modeling on centrifugal compressor flow field predictions. *Journal of Turbomachinery*, **119**, 82–830.

[54] Demirdzic, I. and Peric, M. (1988) Space conservation law in finite volume calculations of fluid flow. *International Journal for Numerical Methods in Fluids*, **8**, 1037–1050.

[55] Demirdzic, I. and Peric, M. (1990) Finite volume method for prediction of fluid flow in arbitrary shaped domains with moving boundaries. *International Journal for Numerical Methods in Fluids*, **10**, 771–790.

[56] Leiben, S., Lewis, G., and Sandercock, D. (1952) Experimental investigation of an axial-flow compressor inlet stage operating at transonic relative mach numbers. *NACA Report RM E52A24*.

[57] T., A., de Rouvroit, L., and Rutherford, A. (1990) Aero-thermal investigation of a highly loaded transonic linear turbine guide vane cascade. *von Karman Institute for Fluid Dynamics. Technical Note 174*.

[58] Swanson, R. and Turkel, E. (1987) Artificial dissipation and central difference schemes for euler and navier-stokes equations. *AIAA paper 87-1107*.

[59] Mavripilis, D. (1987) *Solution of Two-Dimensional Euler Equation on Unstuctured Triangulare Meshes*. Ph.D. thesis, Princeton University, Department of Machanical and Aerospace Engineering.

[60] Mavripilis, D. (1991) Turbulent flow calculations using unstructured and adaptive meshes. *International Journal for Numerical Methods in Fluids*, **13**, 1131–1152.

[61] Ni, R. (1981) Multiple grid scheme for solving the euler equations. *AIAA paper 81-1025*.

[62] Arts, T., Duboue, J., and Rollin, G. (1998(3)) Aero-thermal performance measurements and analysis of a two-dimensional high turning rotor blade. *Journal of Turbomachinery*, **120**, 494–499.

Appendix A

Numerical Implementation

The numerical method used for discretization and solution of viscous flow equations on a moving mesh using the ALE formulation is presented in this chapter. The spatial discretization of the governing equations is performed using a cell-vertex finite volume method on a fully unstructured triangular mesh. Artificial viscosity terms are modified to account for highly stretched elements which are required to capture the details of the flow in the boundary layers and wakes. An explicit Runge-Kutta time-stepping procedure is used to obtain the steady state solution where local time-stepping and implicit residual smoothing are employed for convergence acceleration. The time accurate solution for unsteady calculations is obtained by means of a dual time stepping scheme. Validation of the finite volume method for steady-state flow in 2D turbomachinery cascades is presented in Appendix C.

A.1 Non-dimensionalization

The RANS equations are non-dimensionalized by introducing the dimensionless variables

$$x = \frac{x}{l_{ref}} \quad , y = \frac{y}{l_{ref}} \quad , t = \frac{t}{t_{ref}} \quad ,$$

$$p = \frac{p}{p_{ref}} \quad , T = \frac{T}{T_{ref}} \quad ,$$

$$u = \frac{u}{\sqrt{RT_{ref}}} \quad , v = \frac{v}{\sqrt{RT_{ref}}} \quad , \rho = \frac{\rho}{p_{ref}/RT_{ref}} \quad ,$$

$$\mu = \frac{\mu}{\mu_{ref}} \quad , k = \frac{k}{k_{ref}} \quad , \tag{A.1}$$

where the characteristic length l_{ref} is equal to the axial chord length of the blade and where the physical quantities $p_{ref}, T_{ref}, \mu_{ref}$ and k_{ref} are, respectively, the upstream stagnation pressure and stagnation temperature, the dynamic viscosity and the thermal conductivity.

A.2 Space Discretization

A cell-vertex finite volume scheme is used for discretization of the governing equations on triangular unstructured mesh. The flow variables are stored at the vertices of the triangles and each cell or control volume is formed by taking the union of all triangles meeting at a vertex Fig. A.1

The discretized form of the Eq. 2.1 can be written in this form

$$\frac{d}{dt}\left(\sum_k \Omega_k\right)\mathbf{w}_k + \sum_k \mathbf{Q}_k \mathbf{w}_k = \sum_k \mathbf{D}_k \mathbf{w}_k \tag{A.2}$$

where Ω_k, $\mathbf{Q}_k$, $\mathbf{D}_k$ are respectively the cell area, convective flux balance and viscous contribution for the kth cell surrounding vertex.

The convective flux across an edge can be approximated as the average of the values at its two end points.

$$\mathbf{F}_{AB} = \frac{1}{2}(\mathbf{F}_A + \mathbf{F}_B) \tag{A.3}$$

The net contribution of the convective fluxes for a control volume can then be computed using the relative flow velocities on the cell faces, i.e.

$$Q(\rho)_p = \sum_k [\rho(u-u_g)n_x + \rho(v-v_g)n_y]_k \tag{A.4}$$

$$Q(\rho u)_p = \sum_k [(\rho u(u-u_g)+p)n_x + \rho u(v-v_g)n_y]_k \tag{A.5}$$

$$Q(\rho v)_p = \sum_k [\rho v(u-u_g)n_x + (\rho v(v-v_g)+p)n_y]_k \tag{A.6}$$

$$Q(\rho e)_p = \sum_k [(\rho e(u-u_g)+pu)n_x + (\rho e(v-v_g)+pv)n_y]_k \tag{A.7}$$

where the summation is over all the outer edge of the control volume surrounding vertex p in Fig. A.1 . The formulation amounts to a trapezoidal integration rule around the boundaries of the control surface and is second order accurate.

For the viscous fluxes, an auxiliary control volume is formed by connecting the cell centers, as shown in Fig. A.2. The discrete Gauss theorem is applied once on the each triangle to obtain a numerical approximation to the stress tensor and heat flux vector by computing the required first derivative of the flow variables at the cell centers, i.e.

$$\mathbf{w}_x = \frac{1}{\Omega}\iint \frac{\partial \mathbf{w}}{\partial x}dxdy = \frac{1}{\Omega}\int \mathbf{w}\,dy = \frac{1}{\Omega}\sum_{k=1}^{3}\frac{\mathbf{w}_{k+1}+\mathbf{w}_k}{2}(y_{k+1}-y_k) \tag{A.8}$$

$$\mathbf{w}_y = \frac{1}{\Omega}\iint \frac{\partial \mathbf{w}}{\partial y}dxdy = \frac{1}{\Omega}\int \mathbf{w}\,dx = \frac{1}{\Omega}\sum_{k=1}^{3}\frac{\mathbf{w}_{k+1}+\mathbf{w}_k}{2}(x_{k+1}-x_k) \tag{A.9}$$

where the summation over k refers to the three vertices of the triangle and Ω is the area of the triangle. The divergence of the stress tensor and of the heat flux vector is then obtained directly at the enclosed vertex by a second application of the theorem to the auxiliary control volume which is scaled for consistency, to the computational cell used in convective balance. The average value of the stress tensor σ and heat flux vector $\mathbf{q}$ are used on the edges of the auxiliary control volume. The net viscous contribution of is then recovered in this form

$$D(\rho u)_p = \frac{\Omega}{\Omega'} \sum_{k'} \left[\sigma_{xx} n'_x + \sigma_{xy} n'_y\right]_{k'} \tag{A.10}$$

$$D(\rho v)_p = \frac{\Omega}{\Omega'} \sum_{k'} \left[\sigma_{xy} n'_x + \sigma_{xy} n'_y\right]_{k'} \tag{A.11}$$

$$D(\rho e)_p = \frac{\Omega}{\Omega'} \sum_{k'} \left[(u\sigma_{xx} + v\sigma_{xy} - q_x) n'_x + (u\sigma_{xy} + v\sigma_{yy} - q_y) n'_y\right]_{k'} \tag{A.12}$$

where the summation over k' refers to all the outer edges the auxiliary control volume Ω', shown in Fig. A.2, and $\mathbf{n}' = (n'_x, n'_y)$ is the normal vector to the boundaries of the auxiliary cell. The discretization formulas yields second order accuracy on grids with a smooth variation in the distributions of points.

A.3 Space Conservation Law

By discritizating the space conservation Law, Eq. 2.8 over a moving control volume shown in Fig. A.3, one gets

$$\frac{1}{\Delta t}(\Omega^n - \Omega^o) = \sum_k \left[\mathbf{v}_g \cdot \mathbf{n}^n\right]_k \tag{A.13}$$

where the summation is over all the outer edges of the control volume and $\delta\Omega = \Omega^n - \Omega^o$ is the change of the cell volume during Δt, and superscript n,o denote the

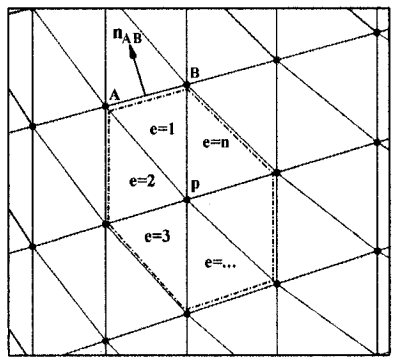

Figure A.1: Domain of influence of node P for a cell-vertex scheme

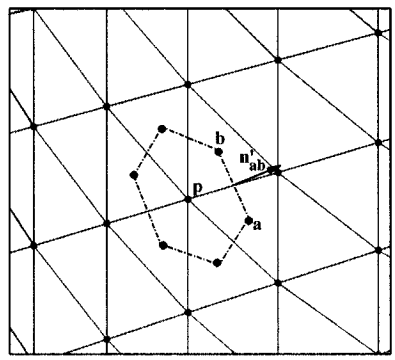

Figure A.2: Auxiliary control volume for discretization of the viscous terms

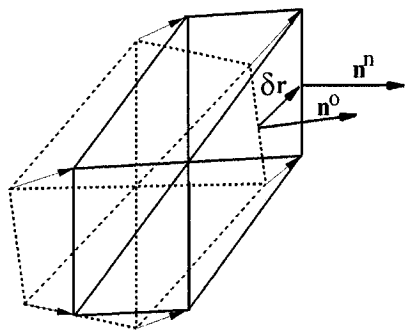

Figure A.3: A moving control volume at two time levels

new and old time levels respectively.

Following Demirdzic and Peric [54], the grid velocities are defined so that the rate of change of the cell volume obtained from is exactly equal to its geometrical rate of change, i.e.

$$u_g = \frac{n_x^o + n_x^n}{2n_x^n} \frac{\delta x_e}{\Delta t} \tag{A.14}$$

$$v_g = \frac{n_y^o + n_y^n}{2n_y^n} \frac{\delta y_e}{\Delta t} \tag{A.15}$$

where δx_e , δy_e are the components of $\delta \mathbf{r}_e$, shown in Fig. A.3. We note that Eq. A.14 is not unique, but rather the most logical way of calculating grid velocities to satisfy SCL. The methodology can be readily applied to three-dimensional grids.

A.4 Artificial Dissipation

In principle, the physical viscous terms of the Navier-Stokes equations are capable of providing the numerical scheme with the dissipative property necessary for stability and capturing discontinuities. However, for high Reynolds-number flows, this can only be achieved by resorting to extremely small mesh spacing throughout the domain. Thus, in practice, it is necessary to introduce artificial dissipative terms to maintain stability in the essentially inviscid portion of the flow field, and to efficiently capture discontinuities. These additional dissipative terms must be carefully constructed to ensure that the accuracy of the scheme is preserved both in the inviscid region of the flow field where the convective terms dominate, as well as in the boundary layer and wake region where the artificial dissipation terms must be much smaller than the physical viscous terms. Previous Navier-stokes solutions on highly stretched meshes [[26, 58]] have demonstrated the need for different scaling of the artificial dissipation terms in the streamwise and normal directions within the regions of viscous flow. However, for unstructured meshes, directional scaling is significantly more difficult to achieve since no mesh coordinate line exist. In fact, unstructured meshes have traditionally been considered to be truly multi-dimensional isotropic constructions with no preferred direction. However, as stated perviously, the efficient solution of high-Reynolds-number viscous flows requires the meshes with highly stretched elements in the boundary layer and wake region, since the physical phenomena are highly directional in nature. For such meshes, even in the unstructured case, a direction and a magnitude of the stretching can be defined for each mesh point, as shown in Fig. A.4. This stretching vector, denoted as $\mathbf{s}$ need not necessarily line up with any of the mesh edges. If the mesh is directly derived from structured quadrilateral mesh by splitting each quadrilateral into two triangles, the

stretching magnitude and direction may be taken as the aspect ratio and the major axis of the generating quadrilateral element for each triangular element respectively. In more general cases, the generation of directionally stretched unstructured mesh requires the definition of local stretching factors throughout the flow field. These can in turn be used to scale the dissipation terms. It is important to note that these stretching vectors represent grid metrics which do not depend on the flow solution.

The artificial dissipation operators on unstructured meshes has previously been constructed as a blend of an undivided pseudo-Laplacian, proposed by Holmes and Connel [25], and biharmonic operator in the flow field [27]. The pseudo-Laplacian for a node is given by

$$\nabla^2(\mathbf{w}_i) = \sum_{k=1}^{n} w_{k,i}(\mathbf{w}_k - \mathbf{w}_i) \tag{A.16}$$

where k represent all neighbors of node i. The weights $w_{k,i}$ are chosen such that the pseudo-Laplacian of a linear function will be zero, as would be the case for true Laplacian. These weights are defined as

$$w_{k,i} = 1 + \Delta w_{k,i} \tag{A.17}$$

where $\Delta w_{k,i}$ are computed as

$$\Delta w_{k,i} = \chi_{x,i}(x_k - x_i) + \chi_{y,i}(y_k - y_i) \tag{A.18}$$

where

$$\begin{aligned} \chi_{x,i} &= \frac{(I_{xy}R_y - I_{yy}R_x)_i}{(I_{xx}I_{yy} - I_{xy}^2)_i} \\ \chi_{y,i} &= \frac{(I_{xy}R_x - I_{xx}R_y)_i}{(I_{xx}I_{yy} - I_{xy}^2)_i} \end{aligned} \tag{A.19}$$

in the above equations R and I represents the first and second moment of inertia of

the control volume in each coordinate direction, that is:

$$\begin{aligned} R_{x,i} &= \sum_{k=1}^{n}(x_k - x_i) \\ R_{y,i} &= \sum_{k=1}^{n}(y_k - y_i) \end{aligned} \tag{A.20}$$

and

$$\begin{aligned} I_{xx,i} &= \sum_{k=1}^{n}(x_k - x_i)^2 \\ I_{yy,i} &= \sum_{k=1}^{n}(y_k - y_i)^2 \\ I_{xy,i} &= \sum_{k=1}^{n}(x_k - x_i)(y_k - y_i) \end{aligned} \tag{A.21}$$

The biharmonic artificial viscosity term is formed by taking the pseudo-Laplacian of ∇w_i

$$\nabla^4 w_i = \sum_{k=1}^{n}(\nabla^2 w_k - \nabla^2 w_i) \tag{A.22}$$

Since the biharmonic operator may be viewed as a Laplacian of a Laplacian, the dissipation operator may be reformulated as a global undivided Laplacian operating on a blend of flow variables and their differences

$$\mathbf{D}(\mathbf{w}) = \Omega\alpha[\mathbf{U}_{xx} + \mathbf{U}_{yy}] \tag{A.23}$$

where

$$\mathbf{U} = \kappa_2'\mathbf{w} - \kappa_4\nabla^2\mathbf{w} \tag{A.24}$$

In the above equations, Ω represent the area of the control volume, which is of the order Δx^2, and $\nabla^2\mathbf{w}$ denotes the undivided Laplacian of $\mathbf{w}$. The first term in the above equation constitutes a relatively strong-order dissipation term which is necessary to prevent un-physical oscillations in the vicinity of a shock. This term

must be turned off in regions of smooth flow. This is accomplished by evaluating κ'^2 at mesh point i as

$$(\kappa_2') = \kappa_2 \frac{\sum_{k=1}^{n} [p_k - p_i]}{\sum_{k=1}^{n} [p_k + p_i]} \tag{A.25}$$

Hence κ_2' is proportional to an undivided Laplacian of the pressure, which is constructed as a summation of the pressure differences along all edges meeting at node i, as depicted in Fig. A.4. This construction has the required property of being of the order unity near a shock and small elsewhere. κ_2 is an empirically determined coefficient which is taken as 0 for subcritical flows, and as 1/2 for transonic and supersonic flows.

In Eq. A.23, the overall scaling of the dissipation is performed by the factor α, which has previously taken as proportional to the maximum eigenvalue of the Euler equations for inviscid flow calculation [27].

Directional scaling of the dissipation may thus be achieved by replacing Eq. A.23 by

$$\mathbf{D}(\mathbf{w}) = \Omega[\alpha_1 \mathbf{U}_{\xi\xi} + \alpha_2 \mathbf{U}_{\eta\eta}] \tag{A.26}$$

where α_1 and α_2 represent different scalings in the ξ and η directions respectively. Here, ξ denotes the direction of the mesh stretching and η the direction normal to ξ. Appropriate expressions for α_1 and α_2 remain to be determined, as well as the discretization procedure for the above operator on unstructured meshes. On structured meshes, the dissipation is often scaled by the maximum eigenvalue of the Euler equations in each coordinate direction, which is given by

$$\lambda_\xi = [|u| + c]\Delta\eta \tag{A.27}$$

$$\lambda_\eta = [|v| + c]\Delta\xi \tag{A.28}$$

where u,v, $\Delta\xi$,$\Delta\eta$ represent the local fluid velocity components and the mesh spacing respectively, in computational space, and c denotes the speed of sound. However,

a more even distribution of the dissipation can be achieved in the two mesh coordinate directions,[26], by replacing the above scaling with

$$\overline{\lambda}_\xi = \phi(r)\lambda_\xi \tag{A.29}$$

$$\overline{\lambda}_\eta = \phi(r^{-1})\lambda_\eta \tag{A.30}$$

where

$$\phi(r) = 1 + r^{2/3} \tag{A.31}$$

and

$$r = \frac{\lambda_\eta}{\lambda_\xi} = \frac{[|v| + c]\Delta\xi}{[|u| + c]\Delta\eta} \tag{A.32}$$

On unstructured meshes, an isotropic value of maximum eigenvalue at each mesh point can be calculated as

$$\lambda = \int_{\delta\Omega} |\mathbf{v} \times \mathbf{dl}| + c|\mathbf{dl}| \tag{A.33}$$

where the integration is performed around the boundary of the control volume for the particular mesh being considered. The discrete approximation of the above integral yields the form for λ

$$\lambda = \sum_{e=1}^{n} |u_{AB}\Delta y_{AB} - v_{AB}\Delta x_{AB}| + c_{AB}\sqrt{\Delta x_{AB}^2 + \Delta y_{AB}^2} \tag{A.34}$$

where Δx_{AB} and Δy_{AB} represent the x and y increments along the outer edge of AB of element e, as shown in Fig. A.1, and u_{AB}, v_{AB} and c_{AB} represent the average values along the edge AB. By considering the equivalent integration around the control volume on a structured quadrilateral mesh, it can be seen that λ approximates the sum of the eigenvalues in the two space dimensions, i.e.

$$\lambda = \lambda_\xi + \lambda\eta \tag{A.35}$$

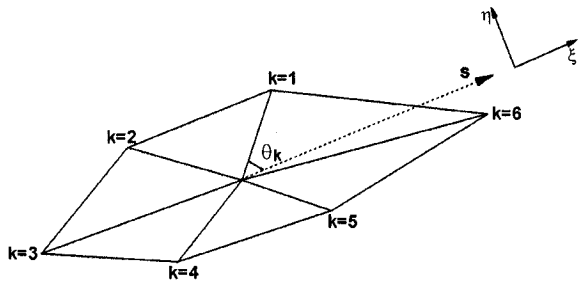

Figure A.4: Definition of local stretching vector for unstructured triangular mesh and the coordinate system associated with stretching directions

Furthermore, the magnitude of the stretching vector **s** on the structured mesh can be considered to be closely related to the cell aspect-ratio. Thus, by analogy with the structured mesh case

$$s \approx \frac{\Delta\xi}{\Delta\eta} \approx \frac{\lambda_\eta}{\lambda_\xi} \tag{A.36}$$

where s represent the magnitude of **s**, and the second approximation assumes that the magnitude of the speed c is much greater than the streamwise and normal velocities u and v in the viscous flow region. Thus, Eqs. A.35 and A.36 permit an estimate of the values of the maximum eigenvalues in the directions parallel and normal to local stretching vector, given the values of λ and s. From Eqs. A.29 through A.32, the α_1 and α_2 coefficients of the of Eq. A.26 are constructed as

$$\alpha_1 = \phi(s)\frac{1}{s+1}\lambda \tag{A.37}$$

$$\alpha_2 = \phi(s^{-1})\frac{s}{s+1}\lambda \tag{A.38}$$

Next, the discretization of the scaled Laplacian of Eq. A.26 on unstructured meshes must be considered. Previously, for inviscid flows [27, 59], the scaled Laplacian of Eq. A.23 was approximated as an accumulated edge difference in computational

space, i.e.

$$\mathbf{U}_{xx} + \mathbf{U}_{yy} = \frac{1}{\Omega} \sum_{k=1}^{n} [\mathbf{U}_k - \mathbf{U}_i] \tag{A.39}$$

where $k = 1, ..., n$ represent the n neighbors of node i, and the difference is taken along all edges meeting at node i. For a cartesian grid this reduces to the familiar five point Laplacian finite difference formula. Equation A.26 can easily be approximated on a cartesian mesh aligned with the ξ and η coordinate directions, simply by multiplying the constructed second differences in the ξ and η directions by α_1 and α_2 respectively. Alternatively, this can be obtained by considering the finite-volume approximation to a Laplacian on a cartesian mesh in a stretched computational space, where $\sqrt{\alpha_1}$ stretching is applied to ξ direction, and $\sqrt{\alpha_2}$ stretching is applied to η direction. By considering the equivalent stretching of computational space for unstructured meshes, a finite-volume approximation to the Laplacian yields the discretization formula for the directionally scaled dissipation operator

$$\mathbf{D}(\mathbf{w}_i) = \Omega |\alpha_1 \mathbf{U}_{\xi\xi} + \alpha_2 \mathbf{U}_{\eta\eta}| = \sum_{k=1}^{n} [\mathbf{U}_k - \mathbf{U}_i] \left[\alpha_1 \cos^2 \theta_k + \alpha_2 \sin^2 \theta_k\right] \tag{A.40}$$

where θ_k represents the angle between the kth mesh edge at node i, and the principal stretching direction ξ, as shown in Fig. A.4. From the above equation, it can be seen that if the kth mesh edge coincides with the ξ or η directions, then the difference along that edge is multiplied by α_1 or α_2 respectively, and if $\alpha_1 = \alpha_2$, then the above discretization reduces to isotropic accumulated edge difference previously employed. Since in practice α_1 and α_2 vary throughout the mesh, equation A.40 is replaced by

$$\mathbf{D}(\mathbf{w}_i) = \sum_{k=1}^{n} [\mathbf{U}_k - \mathbf{U}_i] \left[\frac{A_k + A_i}{2}\right] \tag{A.41}$$

where

$$A_k = \alpha_{1k} \cos^2 \theta_k + \alpha_{2k} \sin^2 \theta_k \tag{A.42}$$

and the i and k subscripts refer to variables evaluated at nodes i and k, thus ensuring a conservative formulation of the dissipation operator.

A.5 Integration to Steady State

The discretization of the spatial derivatives transforms Eq. A.2 into the set of coupled ordinary differential equations

$$\Omega_i \frac{d\mathbf{w}_i}{dt} + [\mathbf{Q}(\mathbf{w}_i) - \mathbf{D}(\mathbf{w}_i)] = 0 \quad i = 1, 2, 3, ..., n \tag{A.43}$$

where n is the number of mesh nodes. The residual $\mathbf{Q}(\mathbf{w})$ represent the discrete approximation to the convective fluxes. $\mathbf{D}(\mathbf{w})$ represents the dissipative terms, i.e. the discrete approximation to the viscous fluxes, as well as the artificial dissipation terms. These equations are integrated in pseudo-time using a five-stage hybrid time-stepping scheme given by

$$\begin{aligned}
\mathbf{w}^{(0)} &= \mathbf{w}^n \\
\mathbf{w}^{(1)} &= \mathbf{w}^{(0)} - \alpha_1 \frac{\Delta t}{\Omega} \left[\mathbf{Q}(\mathbf{w}^{(0)}) - \mathbf{D}_0\right] \\
\mathbf{w}^{(2)} &= \mathbf{w}^{(0)} - \alpha_2 \frac{\Delta t}{\Omega} \left[\mathbf{Q}(\mathbf{w}^{(1)}) - \mathbf{D}_1\right] \\
\mathbf{w}^{(3)} &= \mathbf{w}^{(0)} - \alpha_4 \frac{\Delta t}{\Omega} \left[\mathbf{Q}(\mathbf{w}^{(2)}) - \mathbf{D}_2\right] \\
\mathbf{w}^{(4)} &= \mathbf{w}^{(0)} - \alpha_4 \frac{\Delta t}{\Omega} \left[\mathbf{Q}(\mathbf{w}^{(3)}) - \mathbf{D}_3\right] \\
\mathbf{w}^{(5)} &= \mathbf{w}^{(0)} - \alpha_5 \frac{\Delta t}{\Omega} \left[\mathbf{Q}(\mathbf{w}^{(4)}) - \mathbf{D}_4\right] \\
\mathbf{w}^{n+1} &= \mathbf{w}^{(5)}
\end{aligned} \tag{A.44}$$

where

$$\begin{aligned}
\mathbf{D}_0 &= \mathbf{D}_1 = \mathbf{D}(\mathbf{w}^{(0)}) \\
\mathbf{D}_2 &= \mathbf{D}_3 = \beta\, \mathbf{D}(\mathbf{w}^{(2)}) + (1-\beta)\, \mathbf{D}(\mathbf{w}^{(0)}) \\
\mathbf{D}_4 &= \gamma\, \mathbf{D}(\mathbf{w}^{(4)}) + (1-\gamma)\, \mathbf{D}(\mathbf{w}^{(2)})
\end{aligned} \tag{A.45}$$

$\mathbf{w}^n$ represents the value of the solution vector at the nth time step and $w^{(q)}$ represents the values at the qth stage within a time step. The dissipative operator $\mathbf{D}(\mathbf{w})$ is evaluated only at the first, third, and fifth stages of the scheme, and is employed to construct the subscripted $\mathbf{D}_q$ operator which represents a linear combination of present and previous evaluation of $\mathbf{D}(\mathbf{w})$. This scheme represents a particular case of a large class of multi-stage time-stepping schemes where the coefficients are chosen in order to maintain good stability properties when the viscous terms are dominant, and to ensure large damping of high-frequency errors. The values of these coefficients are taken as

$$\beta = 0.56 \quad \gamma = 0.44$$

and

$$\alpha_1 = 1/4 \quad \alpha_2 = 1/6 \quad \alpha_3 = 3/8 \quad \alpha_4 = 1/2 \quad \alpha_5 = 1$$

A.5.1 Local Time Stepping

Convergence to the steady-state solution may be accelerated by sacrificing the time accuracy of the scheme, and advancing the equations at each mesh point in time by the maximum permissible time step in that region, as determined by local stability analysis. Stability limitation due to both convective and diffusive characters of Navier-Stokes equations must be considered. The local time step is taken as

$$\Delta t = CFL \left(\frac{\Delta t_c \, \Delta t_d}{\Delta t_c + \Delta t_d} \right) \tag{A.46}$$

where CFL is the Courant number of the particular time-stepping scheme, and Δt_c and Δt_d represent the individual convective and viscous time-step limits respectively, the convective time-step limit for Euler equation on unstructured meshes is given

by

$$\Delta t_c = \frac{\Omega}{\lambda_c} \tag{A.47}$$

where Ω denotes the area of the control volume and λ_c represents the maximum eigenvalue of the inviscid equations averaged around the boundary of the control volume, given by

$$\lambda = \sum_{e=1}^{n} |u_{AB}\Delta y_{AB} - v_{AB}\Delta x_{AB}| + c_{AB}\sqrt{\Delta x_{AB}^2 + \Delta y_{AB}^2} \tag{A.48}$$

The viscous time-step limit is taken as

$$\Delta t_d = K_d \frac{\Omega}{\lambda_d} \tag{A.49}$$

where K_d is an empirically determined coefficient which determines the relative importance of the viscous and inviscid time-step limits in the final expressions, and has taken as 0.25 in this work. λ_c and λ_d represent the maximum eigenvalue of the convective and diffusive operators, respectively, averaged about the boundary of the control volume, which for an unstructured mesh in discrete form is given by

$$\lambda_d = \frac{\gamma}{Re\, Pr\, \Omega} \sum_{e=1}^{n} \frac{\mu_{AB}}{\rho_{AB}} [\Delta x_{AB}^2 + \Delta y_{AB}^2] \tag{A.50}$$

where μ_{AB} and ρ_{AB} represent averaged values of viscosity and density along the outer edge AB of each element e, as shown in Fig. A.1.

A.5.2 Implicit Residual Smoothing

The stability range of the basic time-stepping scheme can be increased by implicitly smoothing the residuals. Thus, the original residuals $\mathbf{R}$ may be replaced by the smoothed residuals $\overline{\mathbf{R}}$ by solving the implicit equations:

$$\overline{\mathbf{R}}_i = \mathbf{R}_i + \varepsilon \nabla^2 \overline{\mathbf{R}}_i \tag{A.51}$$

at each mesh point i, where ε is the smoothing coefficient and $\nabla^2\overline{\mathbf{R}}_i$ represents the undivided Laplacian of the residuals which has been previously computed using the pseudo-Laplacian formulation and the geometrical weights [27], so that Eq. A.52 may be written as:

$$\overline{\mathbf{R}}_i = \frac{\mathbf{R}_i + \epsilon \sum_{j=1}^{n} w_{j,i}\overline{\mathbf{R}}_j}{1 + \epsilon \sum_{j=1}^{n} w_{j,i}} \tag{A.52}$$

For highly stretched structured meshes, the use of individual smoothing coefficients in ξ and η mesh coordinate directions which vary locally throughout the mesh, has been found to improve significantly the convergence rate [26]. The use of locally varying smoothing coefficients has the effect of making the scheme more implicit in the direction normal to the boundary layers, or normal to mesh stretching direction, and less implicit in the tangential direction. the implementation of the implicit residual smoothing with locally varying coefficients on unstructured meshes is accomplished by rewriting Eq. A.52 as:

$$\overline{\mathbf{R}}_i = \mathbf{R}_i + \varepsilon_\xi \overline{\mathbf{R}}_{i\xi\xi} + \varepsilon_\eta \overline{\mathbf{R}}_{i\eta\eta} \tag{A.53}$$

where ξ and η now represent the directions tangent and normal to the local mesh stretching vector, as described in the Sec. A.4. By analogy with the structured mesh [26], and making use of Eq. A.36, the smoothing coefficients are taken as:

$$\varepsilon_\xi = \max\left[\frac{1}{4}\left[\left(\frac{CFL}{CFL^*}\frac{1}{s+1}\phi(s)\right)^2 - 1\right], 0\right] \tag{A.54}$$

$$\varepsilon_\eta = \max\left[\frac{1}{4}\left[\left(\frac{CFL}{CFL^*}\frac{s}{s+1}\phi(s^{-1})\right)^2 - 1\right], 0\right] \tag{A.55}$$

$$\tag{A.56}$$

where CFL and CFL^* are the Courant numbers of the smoothed and unsmoothed schemes, respectively, s denoted the magnitude of the stretching vector, and ϕ is

given by Eq. A.31. Since Eq. A.53 now contains a directionally scaled Laplacian, it can be discretized on an unstructured mesh in a manner analogous to that employed for the directionally scaled dissipation operator, as given in Eq. A.40. For economy the resulting set of algebraic equations are solved by performing only two Jacobi iterations.

A.6 Time-Accurate Stepping Scheme

For unsteady flow calculations, the time accuracy of the solution is obtained by means of a dual time stepping scheme, which is presented in this section. Equations A.43 can be discretized implicitly in time as follows

$$\frac{d}{dt}\left[\mathbf{w}^{n+1}\Omega^{n+1}\right] + \mathbf{R}(\mathbf{w}^{n+1}) = 0 \tag{A.57}$$

where $\mathbf{R}$ is the sum of the three flux contributions, and the superscripts denote the time step of the calculation. If we discretize the time derivative term with the implicit second order Gear scheme, we obtain:

$$\frac{3}{2\Delta t}\left[\mathbf{w}^{n+1}\Omega^{n+1}\right] - \frac{2}{\Delta t}\left[\mathbf{w}^{n}\Omega^{n}\right] + \frac{1}{2\Delta t}\left[\mathbf{w}^{n-1}\Omega^{n-1}\right] + \mathbf{R}(\mathbf{w}^{n+1}) = 0 \tag{A.58}$$

This equation for $\mathbf{w}^{n+1}$ is non-linear due to the presence of the $\mathbf{R}(\mathbf{w}^{n+1})$ term and cannot be solved directly. One must therefore resort to iterative methods in order to obtain the solution. The time integration of the discretized Navier-Stokes equations at each time step can then be considered as a modified pseudo-time steady-state problem with a slightly altered residual:

$$\mathbf{R}^{*}(\mathbf{w}) = \frac{3}{2\Delta t}\left[\mathbf{w}\Omega^{n+1}\right] - \frac{2}{\Delta t}\left[\mathbf{w}^{n}\Omega^{n}\right] + \frac{1}{2\Delta t}\left[\mathbf{w}^{n-1}\Omega^{n-1}\right] + \mathbf{R}(\mathbf{w}) \tag{A.59}$$

In this case, the vector of flow variables $\mathbf{w}$ which satisfies the equation $\mathbf{R}^{*}(\mathbf{w}) = 0$ is the $\mathbf{w}^{(n+1)}$ vector we are looking for. In order to obtain this solution vector, we can

reformulate the problem at each time step as the following modified steady-state problem in a fictitious time, t^*

$$\frac{d\mathbf{w}}{dt^*} + R^*(\mathbf{w}) = 0 \tag{A.60}$$

to which one can apply the fast convergence techniques used for steady-state calculations. Applying this process repeatedly, one can advance the flow field solution forward in time in a very efficient fashion.

The time discretization of Eq. A.58 is fully implicit. However, when solved by marching in t^*, stability problems can occur when the stepping in the fictitious time t^* exceeds the physical one. This generally occurs in viscous calculations where core flow cells are much bigger than those close to solid walls. Based on a linear stability analysis, the stepping in t^* must be less than Δt^*_{max} where

$$\Delta t^*_{max} = \min\left[\Delta t^* \,,\, \frac{2CFL^*}{3CFL}\,\Delta t\right] \tag{A.61}$$

After limiting the time step to Δt^*_{max}, the scheme becomes stable and the physical time step Δt can be safely chosen solely on the basis of the accuracy requirement.

Appendix B

Baldwin-Lomax Turbulence Model

The most widespread turbulence models in use currently are either of multiple field equation type or the algebraic type. Field-equation turbulence models are, in principal more general than their algebraic counterparts, and appear well suited for use on unstructured meshes; the additional field equations may be discretized and solved on the unstructured mesh in the same fashion as the governing equations. However, the solution of additional field equations can be quite expensive, especially in the thin boundary layer region near the wall, where the equations can become very stiff. Algebraic turbulence models, on the other hand, are relatively inexpensive to compute, and have demonstrated generally superior accuracy and reliability for limited classes of problems, such as high Reynolds number attached flow over streamlined bodies.

In this work, an algebraic Baldwin and Lomax model [30] is implemented for the closure of the governing equations for its simplicity and success in simulating turbomachinery flows [52, 53]. Description of the model in its original form is presented hereafter.

The model is based on a two layer eddy diffusivity formulation. The effective

turbulent viscosity is taken as:

$$\frac{\mu_t}{\mu_{ref}} = \mu_t^* = \begin{cases} (\mu_t^*)_{inner} & y^* < y^*_{crossover} \\ (\mu_t^*)_{outer} & y^*_{crossover} < y^* \end{cases} \tag{B.1}$$

where y^* is the dimensionless normal distance to the wall and $y^*_{crossover}$ is the minimum value of y^* at which the inner and outer formulation match.

The inner formulation follows the Prandtl-Van Driest formula. Dropping superscript $*$ for clarity, the eddy viscosity coefficient in the inner layer is defined as

$$(\mu_t)_{inner} = \rho\, l^2\, |\omega| \tag{B.2}$$

where

$$l = k\, y\, \left[1 - \exp(-y^+/A^+)\right] \tag{B.3}$$

is the length scale of the turbulence in the inner region, k is a model constant and $|\omega|$ is the magnitude of the vorticity vector and y^+ is the dimensionless distance form the wall consistent with the dimensionless form, defined as

$$y^+ = \frac{\sqrt{\rho_w\, \tau_w}\, y}{\mu_w} \tag{B.4}$$

In the outer part of the boundary layer the following formula is employed

$$(\mu_t)_{outer} = K\, C_{cp}\, \rho\, F_{max}\, y_{max}\, F_{Kleb} \tag{B.5}$$

where K and C_{cp} are model constants and quantities F_{max} and y_{max} are determined by the value and corresponding location of the maximum of the function

$$F(y) = y\, |\omega|\, \left[1 - \exp(-y^+/A^+)\right] \tag{B.6}$$

Due to the potential existence of spurious maxima in $F(y)$, the search for finding the maximum of the function is limited to within y^+ values of 100 and 4000. The Klebanoff intermittency factor F_{Kleb} is given by the following formula

$$F_{Kleb} = \left[1 + 5.5\left[\frac{C_{Kleb}\, y}{y_{max}}\right]^6\right]^{-1} \tag{B.7}$$

Also, transition to turbulence can be modeled by setting a cut off value for the computed eddy viscosity. The suggested criterion is

$$\mu_t = 0 \quad if \quad \mu_{max} < C_{mutm} \tag{B.8}$$

The following values for the model constants are employed

$$\begin{aligned} A^+ = 26 \quad C_{cp} = 1.6 \quad C_{Kleb} = 0.3 \\ k = 0.4 \quad K = 0.168 \quad C_{mutm} = 14 \end{aligned} \tag{B.9}$$

The turbulence length scales, Eq. B.3, which are related to local boundary layer or wake thickness, are determined by scanning the appropriate flow values along specified streamwise locations, referred to as turbulence stations. For structured mesh these lines can be reasonably considered as grid-lines in stream-wise direction. For unstructured meshes, mesh points do not naturally occur at regular streamwise locations. Thus, additional mesh lines normal to the wall boundaries must be constructed and flow variables are interpolated into these lines. The turbulence model is executed on each turbulence mesh line and the resulting eddy-viscosity is transferred back to the computational mesh. This approach is previously used by Mavripilis [60] for external flow. A similar methodology is implemented in this work, where a sheared H-mesh is used as a background mesh for turbulence model. The weighting factors required for interpolation of flow variables and eddy viscosity from one mesh to another are computed and stored in a separate pre-processing routine.

Appendix C

CFD Code Validation

C.1 Bicircular Arc Cascade

This case has been traditionally used for the validation of numerical schemes in two-dimensional turbumachinery cascades. The maximum thickness to chord ratio is 0.2 and spacing to chord ratio is 2. The inviscid ,laminar and turbulent flow conditions are investigated for this configuration and the result are compared to numerical data available in the literature [61, 19, 17].

Fig. C.1(a) shows the sheared H-mesh type grid used for laminar flow calculation. This type of grid is easy to generate and is suitable for relatively thin blades with sharp leading and trailing edges. The spacing between wall and the first vertex is 10^{-3} chord and 1.5×10^{-2} is the minimum spacing in the streamwise direction. For laminar flow calculations the exit Reynolds number $Re_2 = 500$, the exit isentropic Mach number $M_{2is} = 0.5$ and the angle of attack is zero degrees. The isentropic Mach number is computed from the ratio of the local static pressure to the inlet total pressure. Mach number contours for this case are given in Fig. C.2(a) where the maximum Mach number in the domain is 0.754. The flow is separated at about

90 percent chord location as shown in Fig. C.3.

For the transonic turbulent flow the isentropic exit Mach number is $M_{2is} = 0.675$ and Reynolds number is $Re = 10^6$. Figure C.1(b) displays the sheared H-mesh used for the turbulent flow calculations. The minimum mesh spacing at the wall boundary is 2×10^{-4}, and in the x direction a spacing about 1.5×10^{-2} is used to obtain a good representation of the shock wave. The Mach contours presented in Fig. C.2(c), reveal a clean capturing of the shock wave at about 72 percent chord. The flow exhibits separation after the shock wave and then reattaches at about 80 percent of the chord and remains attached on the rest of the blade, as can be seen in Fig. C.3. Figure C.4 shows the convergence history of the L_2 norm of the continuity equation for the inviscid and turbulent flow calculations. The surface variation in the computed isentropic Mach number (M_{is}) for the inviscid and turbulent flow calculations are given in Fig. C.5. The results are in good agreement with numerical results obtained by other researchers [61, 19].

C.2 SNECMA Turbine Rotor Blade

The airfoil investigated in this section is a 2D rotor blade, that is designed and tested at SNECNA [62]. The blade is characterized by a turning of about 110 degree, with an inlet blade angle of 53.36° and an exit blade angle of −65° measured from axial direction.

Figure C.6 shows the unstructured hybrid mesh used for this case with details of the mesh at leading and trailing edges. The hybrid mesh is constructed with 20 layers of hyperbolic structured mesh around the profile, which is converted to triangles and the rest of the domain is filled with Delauney triangular mesh. The minimum normal spacing at the wall is set to 2×10^{-4}.

For the flow analysis, the nominal angle of attack is set to -5 degrees, the exit isentropic Mach number is $M_{2is} = 0.844$ and the Reynolds number is 10^6. Figure C.9 shows a comparison of surface isentropic Mach numbers with experimental data [62]. The results agrees fairly well on the pressure side and suction side of the blade.

Figure C.7 shows the Mach number contours with a close-up near the leading and trailing edge regions. The maximum Mach number in the domain is 1.04 on the suction side of the blade. The streamlines near the leading and trailing edges of the blade are presented in Fig. C.8, which clearly show the stagnation point at the leading edge and the trailing edge vortices.

C.3 VKI-LS89 Transonic Turbine Cascade

This case is a high pressure turbine nozzle guide vane profile, tested at Von Karman Institute [57]. The flow turning is about 70°, the inlet flow angle zero and the spacing to chord ratio is 0.85.

Figure C.10 shows the unstructured hybrid mesh used for this case with details of the mesh at leading and trailing edges. The hybrid mesh is constructed with 25 layers of hyperbolic structured mesh around the profile, which is converted to triangles and the rest of the domain is filled with Delauney triangular mesh. The minimum normal spacing at the wall is set to 1.2×10^{-4}.

For the flow analysis, the Reynolds number is 10^6 and exit isentropic Mach numbers M_{2is} of 0.875 and 1.02 are investigated. Blade isentropic Mach number distributions are presented in Fig. C.13 as function of a reduced coordinate (s/c) measured along the profile surface and are compared with the experimental results [57]. The flow steeply accelerate along the suction side up to (s/c = 0.3). A small plateau (s/c = 0.35-0.4) is followed by a re-acceleration. For the lower exit Mach

number $M_{2is} = 0.875$, the velocity distribution is then rather flat. For the higher exit Mach number $M_{2is} = 1.02$, the flow accelerate up to (s/c = 0.85-0.95). A shock is then observed $s/c = 1.05$. The velocity distribution along the pressure side varies smoothly, with no existence of a velocity peak downstream of the leading edge. The Mach contours for both cases are shown in Fig. C.11. The streamlines resulting from the flow analysis at the lower exit isentropic Mach number $M_{2is} = 0.875$, are also shown in Fig. C.12 which clearly show the leading edge stagnation point and the von Karman vortices at the trailing edge of the blade.

(a)

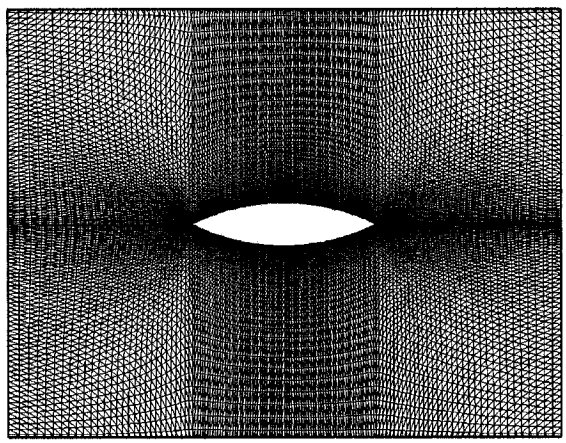

(b)

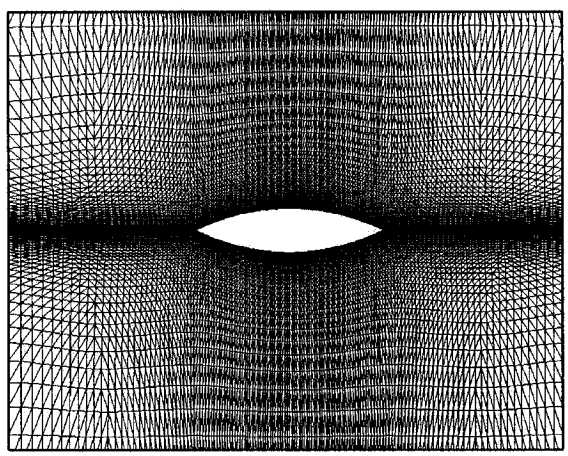

Figure C.1: The computational grid for bicircular cascade 138×100
(a)Laminar flow (b)Turbulent Flow

(a)

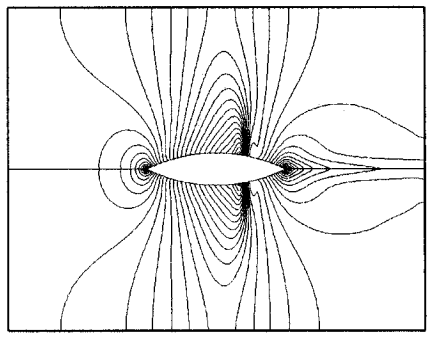

(b)

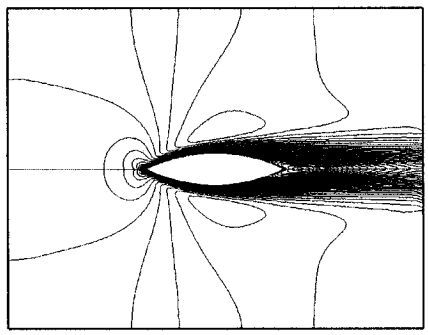

(c)

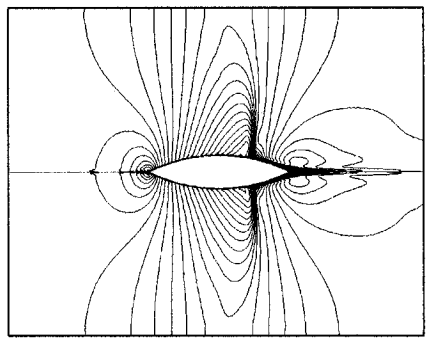

Figure C.2: Mach number contours for bicircular cascade
(a)Inviscid flow $M_{2is} = 0.675$ (b) Laminar Flow $M_{2is} = 0.5, Re = 500$, (c)Turbulent flow $M_{2is} = 0.675, Re = 10^6$

(a) (b)

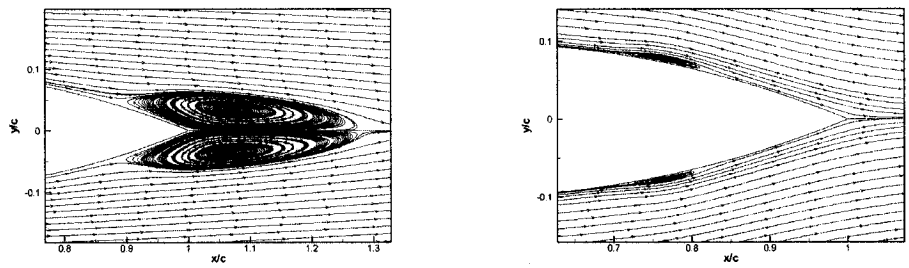

Figure C.3: Streamlines for bicircular cascade
(a)Laminar Flow (b) Turbulent flow

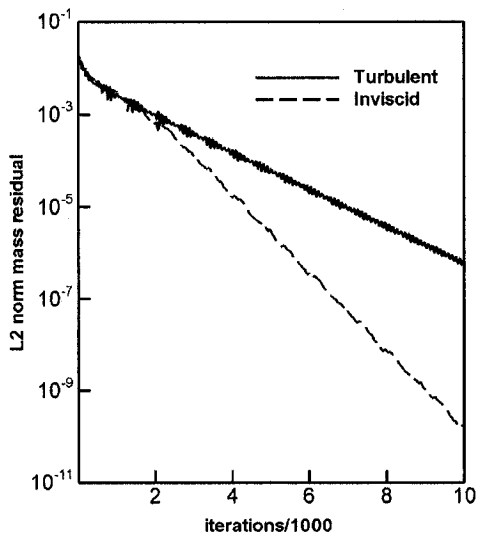

Figure C.4: Convergence history for bicircular cascade

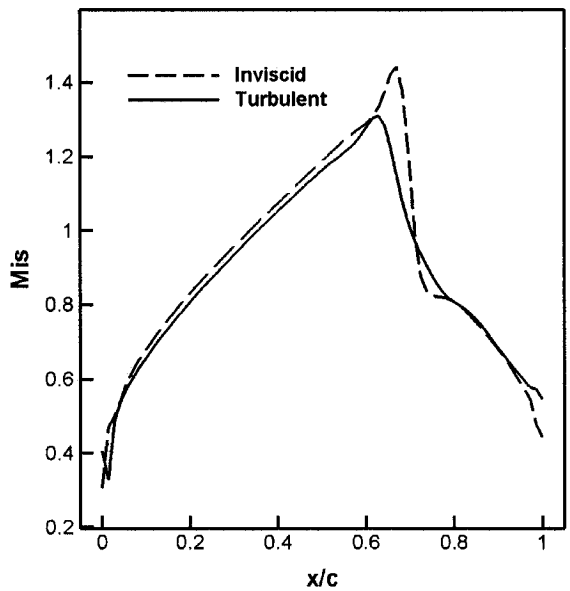

Figure C.5: Isentropic Mach number distributions for bicircular cascade

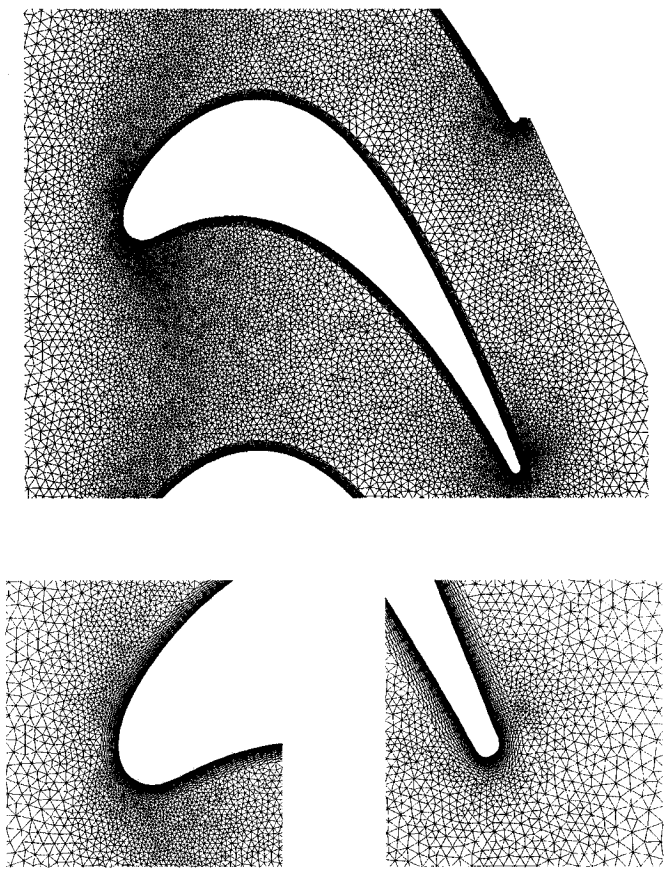

Figure C.6: Hybrid unstructured grid for SNECMA cascade

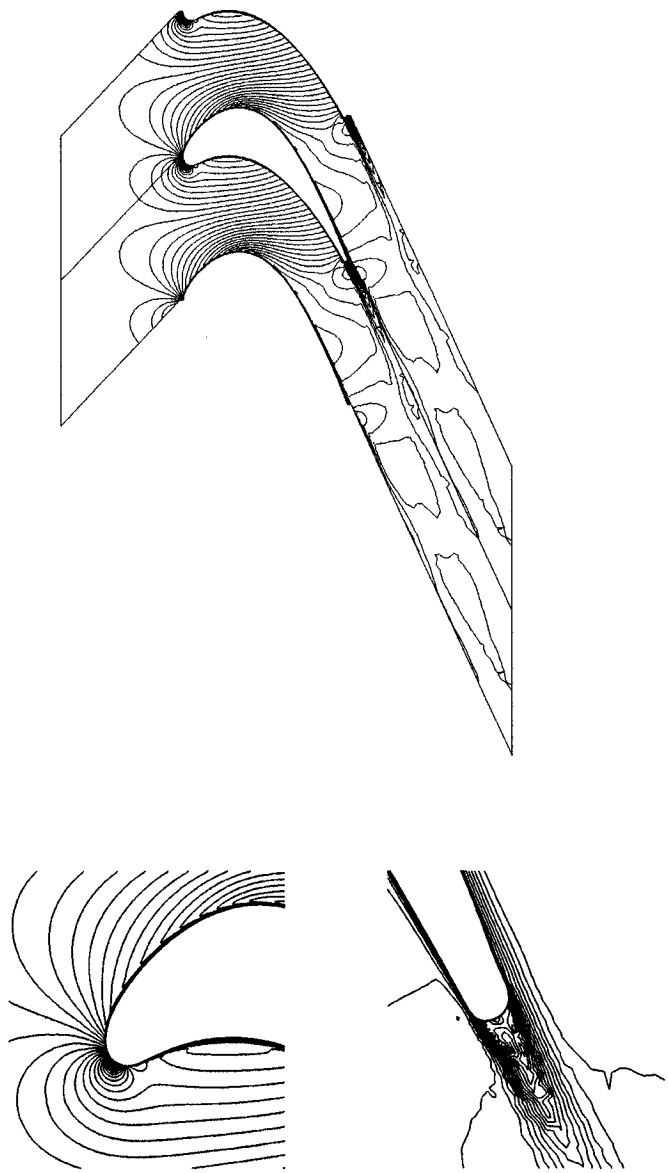

Figure C.7: Mach number contours for SNECMA cascade
$M_{2is} = 0.844, Re = 10^6$

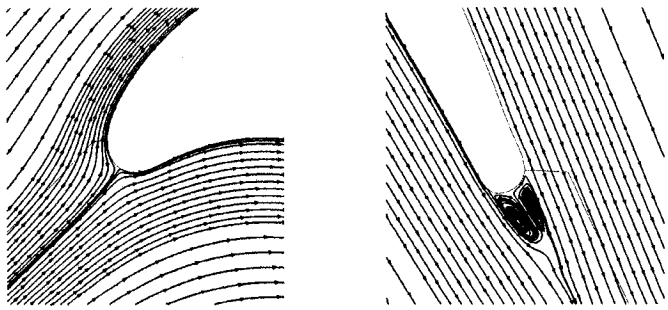

Figure C.8: Streamlines at leading and trailing edge of SNECMA cascade

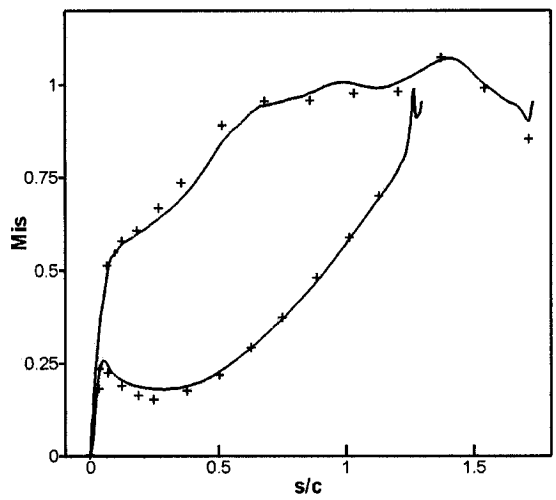

Figure C.9: Isentropic Mach number distribution for SNECMA cascade

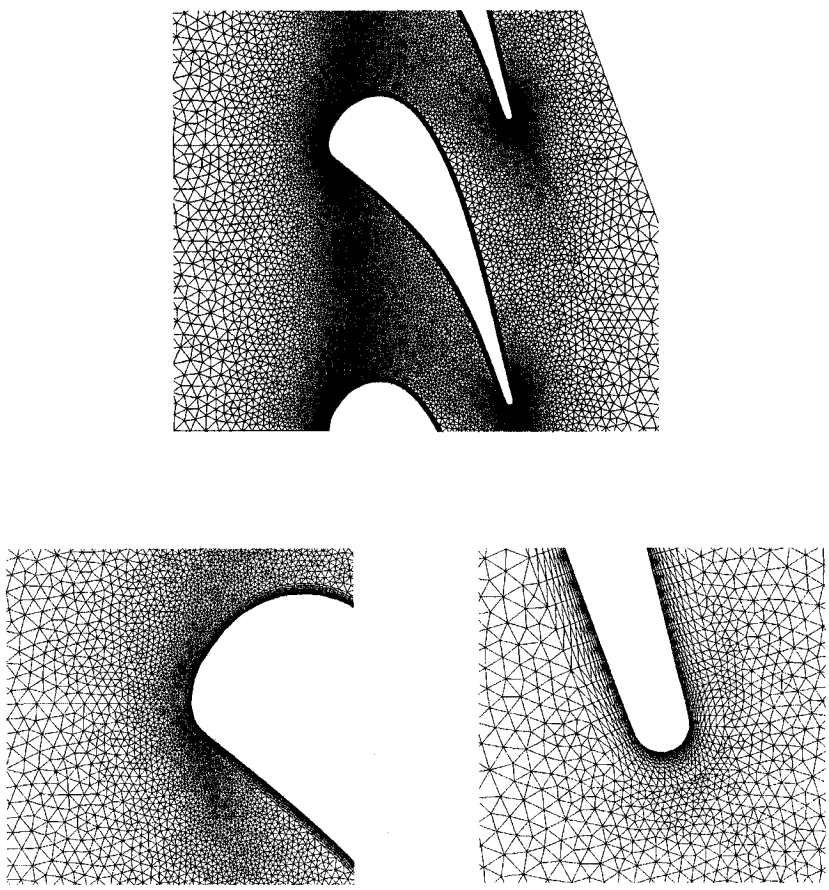

Figure C.10: The hybrid unstructured mesh for VKI cascade

(a) (b)

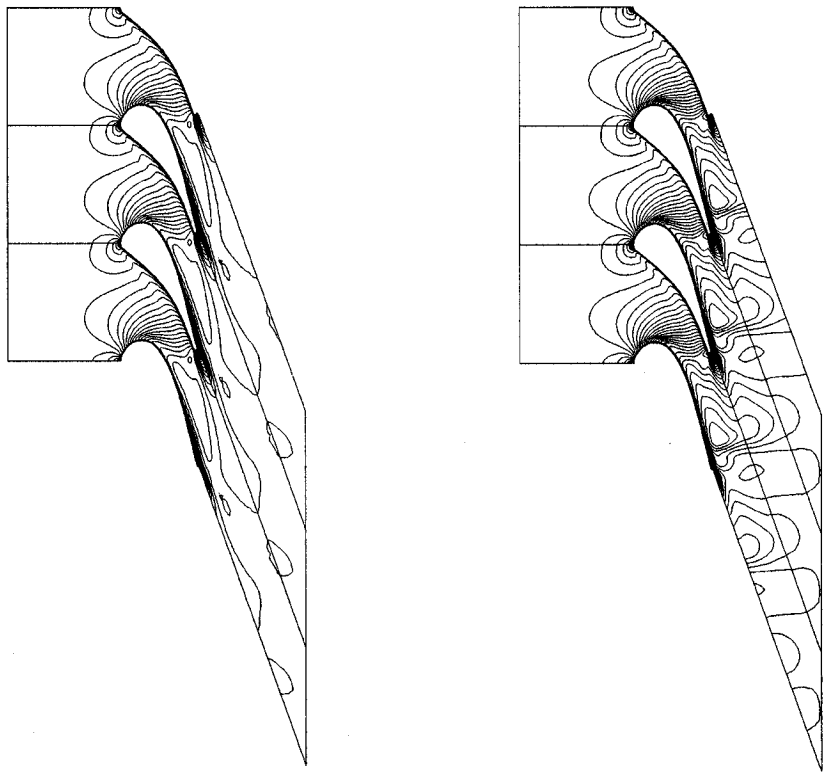

Figure C.11: Mach number contours for VKI cascade
(a)$M_{2is} = 0.875$, (b)$M_{2is} = 1.02$

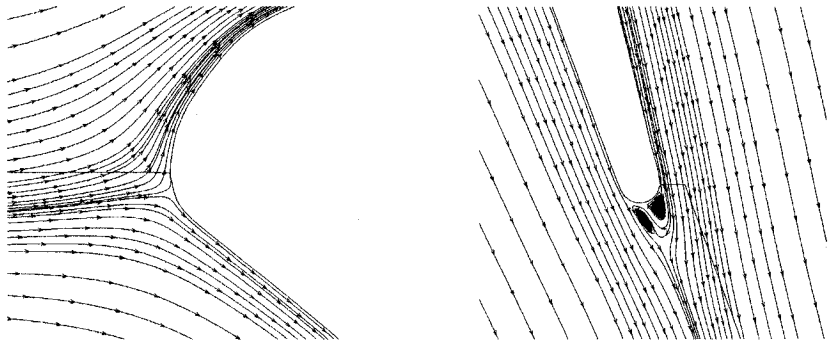

Figure C.12: Streamlines at near LE and TE regions of VKI cascade

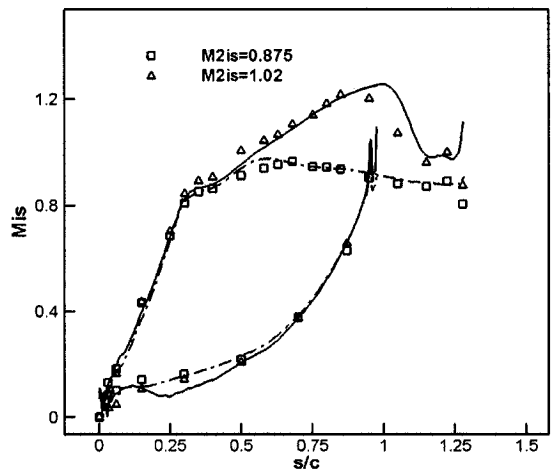

Figure C.13: Isentropic Mach number distributions for VKI cascade

Appendix D

Stability Analysis

An analysis of the wall movement scheme stability shows that the predicted wall velocity must be heavily under-relaxed in order to provide overall stability of the algorithm. Consider for example the situation shown in Fig. D.1(a) where the correct wall geometry has been obtained for all but one point, j. The calculated wall slop at point j and its neighbors using central difference scheme is also shown in Fig. D.1(a). After the next time step if the flow is supersonic, the new wall pressure will be higher than specified at point j-1 and lower than specified at point j+1. New wall positions will be assigned as in Fig. D.1(b). After the next time step, the calculated wall pressure will become lower than specified, causing the point j to move towards its correct position.

As may be seen, the assumed error at point j induces a position error at points j-1 and j+1. For the solution process to converge, these induced errors must be smaller than the original position error. Referring to Fig. D.1(a) and assuming small deflections, the induced error will be :

$$\Delta h_i = \Delta t \omega' \sqrt{\frac{dp}{\rho}} < \Delta h \tag{D.1}$$

where ω is an under-relaxation factor.

Numerical experiment has shown that the relaxation factor itself should be chosen to be proportional to $1/a\sqrt{dp/\rho}$ for best convergence rate, where a is the speed of sound. Choice of this relaxation parameter eliminated small geometry oscillations which retard global convergence. We may now write Eq. D.1 as:

$$\Delta t \omega \frac{1}{a} \frac{dp}{\rho} < \Delta h \tag{D.2}$$

For small deflection, linearized supersonic flow analysis gives

$$\frac{dp}{\rho} = \frac{M^2}{\sqrt{M^2-1}}\theta = \frac{M^2}{\sqrt{M^2-1}} \frac{\Delta h}{2\Delta x} \tag{D.3}$$

Therefore the Eq. D.2 becomes:

$$\Delta t \frac{1}{a} \frac{\gamma M^2}{\sqrt{M^2-1}} \frac{\Delta h}{2\Delta x} < \Delta h \tag{D.4}$$

or

$$\omega \frac{\Delta t}{\Delta x} \frac{1}{2a} \frac{M^2}{\sqrt{M^2-1}} < 1 \tag{D.5}$$

If we set the CFL number, $\Delta t/\Delta x(u+a)$ equal to 1.0, we may rewrite this as :

$$\omega < 2 \frac{\sqrt{M^2-1}}{M(M+1)} \tag{D.6}$$

This analysis shows that the wall update scheme should be strongly under-relaxed in order to provide overall stability when the flow is everywhere supersonic. ω approaches zero slowly as M goes to one, for example $\omega < 0.19$ for $M = 1.02$. A similar discrete node stability analysis for subsonic flow shows that the wall update scheme is also stable for subsonic flow.

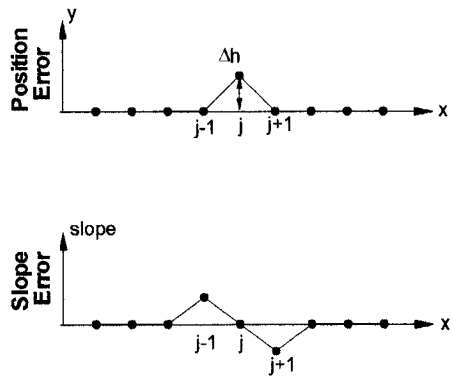

(a)Idealized initial geometry error

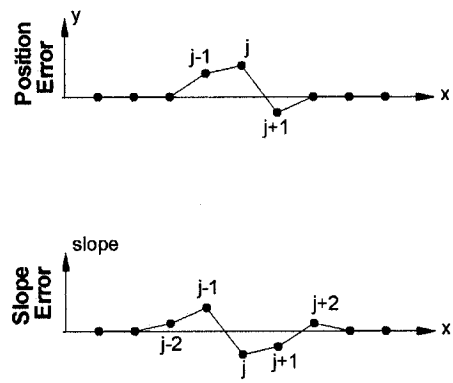

(b)Idealized Intermediate geometry error

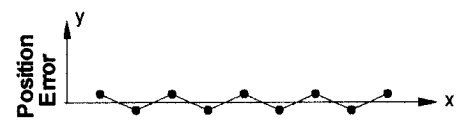

(c)Idealized final geometry error

Figure D.1: Stability analysis of the wall movement